Journal of Theoretical Biology 595 (2024) 111941

Contents lists available at ScienceDirect

Journal of Theoretical Biology

journal homepage: www.elsevier.com/locate/yjtbi

Simple olfactory navigation in air and water

Bowei Ouyang [a], Aaron C. True [b], John P. Crimaldi [b], Bard Ermentrout [a,*]

[a] Department of Mathematics, University of Pittsburgh, Pittsburgh, PA 15260, United States of America
[b] Civil, Environmental, and Architectural Engineering, University of Colorado Boulder, Boulder, CO 80309, United States of America

ARTICLE INFO

Keywords:
Klinotaxis
Tropotaxis
Animal navigation
Olfaction
Computational modeling

ABSTRACT

Two simple algorithms based on combining odor concentration differences across time and space along with information on the flow direction are tested for their ability to locate an odor source in four different odor landscapes. Image data taken from air plumes in three different regimes and a water plume are used as test environments for a bilateral ("stereo sampling") algorithm using concentration differences across two sensors and a "casting" algorithm that uses successive samples to decide orientation. Agents are started at random locations and orientations in the landscape and allowed to move until they reach the source of the odor (success) or leave the imaged area (failure). Parameters for the algorithm are chosen to optimize success and to minimize path length to the source. Success rates over 90% are consistently obtained with path lengths that can be as low as twice the starting distance from the source in air and four times the distance in the highly turbulent water plumes. We find that parameters that optimize success often lead to more exploratory pathways to the source. Information about the direction from which the odor is coming is necessary for successful navigation in the water plume and reduces the path length in the three tested air plumes.

1. Introduction

Olfaction–the ability of animals to detect odors–is the most ancient sense in animals and is fundamental in allowing them to navigate towards food, mates, home nests, and away from predators and other dangers (See Reddy et al. (2022) for a recent review). The ability to navigate using olfactory cues is crucial for animals in various ecological contexts, such as foraging, mating, and territoriality, and has implications for their survival and reproductive success. Animals are able to gain information about their environment by sensing chemicals in air and water despite the complex spatial and temporal structures of turbulent plumes (Crimaldi, 2008; Connor et al., 2018).

Odor plumes contain information, both as to the quality of the odor, and more importantly for our purposes, about the location of the source (Boie et al., 2018) and animals have devised many strategies to utilize this information. One key aspect of olfactory navigation is the perception and processing of odor cues, which serve as critical signals for animals to orient themselves in space. Studies have shown that animals can detect and discriminate different odors with remarkable sensitivity and specificity (Laska, 2017; Bhattacharyya and Bhalla, 2015). Olfactory cues from the environment, such as odor plumes, can provide valuable information about the location, direction, and distance of a target or a resource, allowing animals to navigate in complex and dynamic environments (Gadenne et al., 2016; Martin et al., 2011).

Moreover, olfactory navigation involves sophisticated neural processing mechanisms that allow animals to integrate and interpret olfactory cues to generate spatial representations and form cognitive maps of their environment. Experimental studies have revealed the involvement of specific brain regions, neural circuits, and neurotransmitters in the processing of olfactory information and the generation of navigational behaviors (Abraham et al., 2014; Weiss et al., 2008).

Furthermore, behavioral studies have revealed a variety of navigation strategies employed by animals, ranging from simple innate responses to complex learned behaviors. Animals can exhibit innate behaviors, such as following odor gradients or utilizing stereotypical patterns of odor search, as well as learned behaviors, such as associative learning and memory-based navigation (Bhattacharyya and Bhalla, 2015; Martin et al., 2011).

Animals use numerous algorithms that enable them to locate the source of an odor in natural and experimental settings which exploit the spatio-temporal aspects of odor plumes (Vickers, 2000; Baker et al., 2018). For example, odor plumes widen with distance from the source so that animals who lose the plume instinctively backtrack downstream in order to capture the plume (Álvarez-Salvado et al., 2018). Crabs

* Corresponding author.
E-mail addresses: BOO5@pitt.edu (B. Ouyang), aaron.true@colorado.edu (A.C. True), crimaldi@colorado.edu (J.P. Crimaldi), phase@pitt.edu (B. Ermentrout).

https://doi.org/10.1016/j.jtbi.2024.111941
Received 18 December 2023; Received in revised form 27 August 2024; Accepted 1 September 2024
Available online 11 September 2024

exploit the plume shape by combining flow direction with plume edge detection to locate clam odors in experimental studies (Webster and Weissburg, 2001). In turbulent flow, the rate of encountering high concentrations of odorant increases near the source, thus some animals use the rate of encounters as a guide to an odor source (Rigolli et al., 2022a; Michaelis et al., 2020; Demir et al., 2020; Park et al., 2016). Among the simplest algorithms are those which depend on changes in concentration. Many animals with bilateral body plans use sensors on either side of the body to compare odor concentration and steer in the direction of greater odor. This is called *tropotaxis* or *stereo-olfaction.* Sharks (Kajiura et al., 2005), mice (Jones and Urban, 2018), rats (Rajan et al., 2006), moles (Catania, 2013), flies (Louis et al., 2008), and even humans (Wu et al., 2020) have all been shown to use left–right comparison of odors to follow plumes to their source and to follow odor trails. This "bilateral" strategy has also been used to guide robots (Gumaste et al., 2020) and can enhance other algorithms (Louis et al., 2008). Sampling a plume at two successive times in different locations (*klinotaxis*) is another common strategy that allows an animal to widen the spatial difference for comparison. Mice (Liu et al., 2020; Findley et al., 2021), bats (Brokaw et al., 2021), and moles (Catania, 2013) all employ this type of strategy to move toward a desired odor source. These relatively simple algorithms (here after called respectively *bilateral* and *casting*) have an advantage of being computationally simple and thus easy to implement through neural circuits (see Discussion) and in robotic applications. We want to be clear that in this paper we are using the term "casting" as a shorthand name for the strategy in which the agent samples odor by swinging its sensor alternately from left to right in successive steps. Thus, it is not the same as the casting by moths and other insects that sweep back and forth orthogonal to an odor plume.

The algorithms described in the previous paragraph are based primarily on differences in concentration. However, there are a number of model-based strategies that have been shown to be successful, particularly in turbulent environments. Perhaps the most well-known of these is *infotaxis* (Vergassola et al., 2007) which is especially good in cases where encounters with odors are rare. This strategy keeps an internal estimate of the location of the source which is updated with each sample; cases with either no odor or odor provide useful information. A recent innovation in search strategies is the *finite state controller* (Verano et al., 2023) which compresses memory of past decisions into probabilistic transition between states, while still depending on sensory inputs. A recent review (Reddy et al., 2022) describes these probabilistic algorithms as well as algorithms that are based on concentration differences.

In previous papers (Liu et al., 2020; Hengenius et al., 2021) we explored the efficiency and accuracy of bilateral and casting algorithms on synthetic odor landscapes and in imaged air plumes with fixed parameters based on observations of mice locating spots (Liu et al., 2020). In this paper, we further analyze these two algorithms, which use only local (in space and time) concentration information and additionally, the ambient flow direction to follow diverse plumes in air and water in order to locate the source of the odors. These plumes differ in the spatiotemporal structure of their odor concentration fields (shown in detail in Connor et al. (2018) and Ritsch (2019), respectively). That structure is quantified in key metrics like the statistical moments of the concentration field and the signal intermittency (fraction of time the signal is non-zero, related to the intensity of concentration fluctuations about the mean (Wilson et al., 1985; Nironi et al., 2015)). These quantities are local in space, varying with distance from the source both in the mean flow direction and transverse to the flow (Crimaldi et al., 2002), and are important shape parameters describing the spatially-varying probability distribution function of the concentration field (Yee, 1990; Celani et al., 2014; Nironi et al., 2015) (Gamma-like in diverse turbulent flows). Unique odor landscapes thus encode information about the source location differently through characteristic spatiotemporal structure. The navigational relevance of different structural cues, like intermittency, is an active area of research, including understanding the neural, behavioral, and physical bases (Liao and Cowen, 2002; Lei et al., 2009; Michaelis et al., 2020; Gumaste et al., 2024). Navigating agents are thus presented with unique challenges in which different canonical search behaviors are likely more well-suited both in different odor landscapes and with varying distance from the source (Rigolli et al., 2022b). To appreciate the differences in the air and water plumes here, as well as among different plumes within air or water, it is helpful to consider the physical processes acting on odor packets en route from source to sensor and the fluid dynamic parameters involved.

Odor are advected downstream with the mean flow while spreading out under the influence of molecular diffusion which acts to destroy concentration gradients. Odor diffusivities in air are approximately a thousand times more diffusive than their aqueous counterparts, suggesting rapid destruction of odor concentration gradients. However, packets are also stretched and folded by fluid dynamic strain arising from spatial gradients in the flow field which locally sharpens concentration gradients. The net effect of these competing processes is broadly referred to as mixing (Ottino et al., 1990; Roberts and Webster, 2002; Villermaux, 2019) and scale-dependencies arise in turbulent mixing because of the broad range of length and time scales involved (Taylor, 1922; Richardson, 1926). This gives rise to the dynamic and intermittent characteristics intuitively associated with turbulent odor plumes.

Mixing produces diverse odor landscapes, and in the broadest terms, this diversity arises from differences in i. the spatiotemporal structure of the transporting flow and ii. the nature of the odor source itself (Murlis et al., 1992, 2000; Cassiani et al., 2020; Crimaldi et al., 2022). In fluid dynamic terms, diversity in plume statistics reflects differences in dimensionless quantities that parameterize the equations governing describing the flow (continuity and Navier–Stokes equations) and odor transport and dispersion (coupled advection–diffusion equation). These include the Reynolds number Re describing the relative importance of inertial and viscous flow effects and Schmidt number Sc describing the relative importance of fluid momentum versus odor diffusivities. Intuitively, the Pèclet number Pe (= ReSc) describes the relative importance of advective to diffusive scalar transport mechanisms. Variations in Re and Pe set the relative importance of molecular diffusion and fluid dynamic strain acting on odor packets from source to sensor. These parameters, together with other dimensionless quantities describing the configuration of the source (Nironi et al., 2015) (e.g. its size relative to large eddies in the flow (Fackrell and Robins, 1982), its momentum and buoyancy relative to the transporting flow (Hunt and Van den Bremer, 2011), its proximity to solid boundaries (Connor et al., 2018)) define mixing regimes present both near the source and farther downstream. These regimes in turn set the spatiotemporal structure of the odor concentration field which encodes exploitable information about the source location. Understanding the physical processes driving the evolution of the concentration field and the fluid dynamic parameters that broadly set the spatiotemporal structure of odor signals (Moore and Crimaldi, 2004; Riffell et al., 2008) provides a more unified intuition on optimal olfactory navigation strategies in diverse naturalistic contexts (Reddy et al., 2022).

To test navigation algorithms in diverse odor landscapes, we used four experimental plume datasets (three in air and one in water) with diverse concentration statistics owing to differences in the Reynolds number, Schmidt number, and source configuration (see Section 2 and Table A.5). We varied a range of parameters in order to optimize the success in locating the plume and to minimize the total path length to get to the plume. We show that the two goals (roughly, accuracy versus speed) need not be in complete opposition and in some plumes can even be correlated. We combine either of the two local algorithms along with some noise in the heading and a term that depends on the flow direction and the concentration of the odorant to find parameter sets that lead to optimal success and minimal path-length (tortuosity). We compare and contrast optimal parameters in the different air plumes

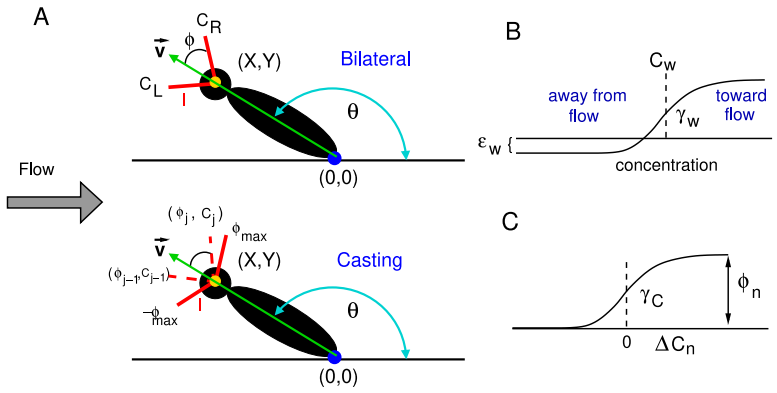

Fig. 1. (A) Coordinates and variables for the two algorithms. Position in the plane is (X, Y) (yellow spot), orientation is θ, forward velocity is $\vec{v}$. l is sensor length, ϕ is sensor angle: fixed for bilateral and variable for casting. Air/water flow is from the left. C is the concentration at the sensor tip. (B) Concentration sensitive modulation of the bias toward or away from the direction of the flow (C) Concentration sensitive heading for the casting model.

as well as the water plume. Finally, we discuss possible strategies in which the parameters of the algorithms might vary depending on the circumstances and how these parameters relate exploration and stability. We also suggest possible neural circuits that could be used to implement the algorithms.

2. Methods

2.1. Plume datasets

Testbed experimental datasets summarized in Table A.5 were obtained from planar laser-induced fluorescence (PLIF) measurements of passive scalar plumes made in a low-speed wind tunnel (air) and an open-channel flume (water). These datasets are described in detail in the appendix and provided time-resolved scalar (odor) concentration fields over fields-of-view (FOV) spanning tens to hundreds of odor source diameters, at sub-millimeter spatial resolutions. Variations in experimental configurations, including mean flow speed, turbulence intensity, ambient fluid, and source characteristics (size, injection rate, proximity to solid boundaries) produced a range of plumes whose concentration statistics mimic those in naturalistic plumes relevant to diverse olfactory contexts.

Navigational algorithms were tested in three air plume datasets with varying mean flow speeds and odor source configurations; experimental parameters are summarized in Table A.5 for each dataset. Two datasets featured isokinetic odor releases in a freestream configuration (i.e. on the tunnel centerline far from solid boundaries) with mean flow speeds of 5 and 20 cm/s, respectively. The third dataset featured an isokinetic odor release with a mean flow speed of 10 cm/s in a near-bed configuration, where a false floor was placed directly below the release tube and spanned the full length and width of the test section. All datasets were collected in segments of 4 min and consisted of 32 400, 18 000, and 36 000 total frames, respectively.

Navigational algorithms were also tested in one water plume dataset with a mean flow speed of 5 cm/s with an isokinetic odor release in a freestream configuration through a round tube (0.69 cm diameter). The dataset was collected in segments of 22 s and consisted of 40 000 total frames.

2.2. Algorithms

We consider two different types of local algorithms: bilateral search and temporal comparison ("casting"). Fig. 1A illustrates the geometry of the two algorithms. We track three variables, the spatial location at time step, n, (X_n, Y_n), and the heading, θ_n. Throughout this paper, we will use the terms heading and orientation synonymously to mean the angle θ_n of the agent. Each algorithm has the form:

$$X_{n+1} = X_n + \Delta t\ v \cos\theta_n \tag{1}$$

$$Y_{n+1} = Y_n + \Delta t\ v \sin\theta_n \tag{2}$$

$$\theta_{n+1} = \theta_n + \Delta t\ W_n + D_n + \sigma N(0,1)\sqrt{\Delta t}. \tag{3}$$

Here, $N(0,1)$ is a normally distributed random variable with mean 0 and variance 1 and v is the absolute speed of the agent, Δt is the sampling time for the plumes; for air plumes, $\Delta t = 1/15$ seconds and for the water plumes, it is 1/45 s.

2.2.1. Flow sensitive component

W_n is a component which takes into account the flow direction, so that it tends to bias the agent either upstream (when an odor is detected) or downstream (when there is no odor). Since the plume always originates at the left (upstream) end of the domain,

$$W_n = A_w \left(\frac{1}{1+\exp(-\gamma_w(C_n - C_w))} - \epsilon_w \right) \sin\theta. \tag{4}$$

Here, C_n is a local concentration (the average of the two sensors for the bilateral algorithm and the concentration at the single sensor for casting) and $A_w, \gamma_w, C_w, \epsilon_w$ are parameters. If the flow component is positive, then θ will be biased toward π (upstream and to the left end of the domain) while if it is negative, θ will be biased toward 0 (downstream or to the right). This term is illustrated in Fig. 1B. The parameter A_w represents the overall strength of the modulation and has dimensions of radians/second. A_w multiplies a second term that is concentration dependent. The parameter $\epsilon_w \geq 0$ determines the concentration below which the agent will reverse direction and move downstream. The parameters, γ_w, C_w determine the overall shape of the concentration dependence as shown in the figure.

2.2.2. Bilateral component

D_n is the part of the algorithm that uses either spatial (bilateral) differences in concentration or temporal (casting) differences. The bilateral algorithm (see diagram) is

$$D_n = \Delta t \beta (C_L^n - C_R^n) \tag{5}$$

$$C_L^n = C(X_n + l\cos(\theta_n + \phi), Y_n + l\sin(\theta_n + \phi), n\Delta t)$$

$$C_R^n = C(X_n + l\cos(\theta_n - \phi), Y_n + l\sin(\theta_n - \phi), n\Delta t)$$

where $C(x, y, t)$ is the concentration (or transformed concentration) at position (x, y) in the plume and time t and l, ϕ are the length and angle from the midline of the two sensors (See Fig. 1A.) The parameter β describes the sensitivity of the change in heading to the difference between the two sensors. Larger values of β mean more sensitivity. As the concentration is normalized, β has units of radians/second.

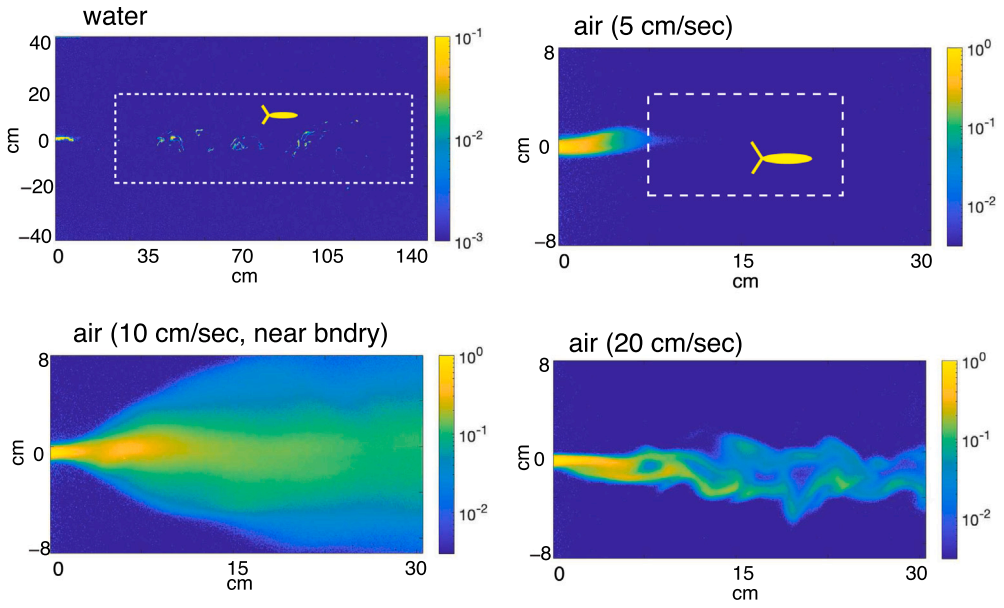

Fig. 2. The odor landscapes. Log concentrations are shown for clarity. Dashed boxes indicate the sampled starting locations. The scale of the maximal sensor length is shown in the upper two plots. See text for detailed descriptions.

2.2.3. Casting component

The casting algorithm chooses an angle, $\phi_n = (-1)^n \phi_{max} U_n$ where U_n is a uniformly distributed random number in $(0, 1)$ and updates the heading:

$$D_n = \frac{\phi_n}{1 + \exp(-\gamma_c [C_n - C_{n-1}])} \qquad (6)$$
$$C_n = C(X_n + l\cos(\theta_n + \phi_n), Y_n + l\sin(\theta_n + \phi_n), n\Delta t).$$

Thus, the new heading will move toward $\theta_n + \phi_n$ if the new concentration exceeds the previous concentration. The function governing the degree of motion is illustrated in Fig. 1C. The parameter γ_c determines how sensitive the algorithm is to the difference in two successive samples.

2.2.4. Concentration transformation

Because the plume concentrations vary over several orders of magnitude, we transform the concentration by applying a simple Hill function:

$$C = \frac{c}{c + C_{hill}} \qquad (7)$$

where c is the raw concentration (from the plume image) and C_{hill} is chosen to be the mean concentration over the total set of frames and plume area. Our previous work on air plumes (Boie et al., 2018) has shown that this transformation maximizes information about the location of the plume. Essentially, this shifts the maximal sensitivity to concentrations that are above the background.

2.3. Simulations

An agent is randomly placed in the domain of the plume image with an initial heading taken randomly from the interval $(\pi/2, 3\pi/2)$, that is, heading upstream. (X_0, Y_0, θ_0) are chosen using Latin hypercube sampling (McKay et al., 2000). The agent moves at a constant speed until the stopping criterion is reached. If the agent gets within R_0 pixels of the source, then the trial is marked as a success and we store n the number of steps. For the three air plumes, R_0 is 5 pixels or 3.75 mm. For the water plume, R_0 is 10 pixels or 5.8 mm. For the present study, we employed the *Hard fail* boundary condition: if (X_n, Y_n) exits the image domain, then the simulation ends and it is marked as a failure. In prior work (Liu et al., 2020; Hengenius et al., 2021), we allowed for *reflecting* boundaries to mimic experiments where the agent (in this case a mouse) is confined in an arena. Here, we only employ the hard fail, which sets a lower bound for success rate. If the number of frames is exceeded (3500 for air, 40 000 for water), then the trial is marked as a failure. To test the efficacy of a given algorithm and parameter set, we run N_T trials with the agent started at a random location in a rectangle around the plume. We track the fraction success, $\#N_{succ}/N_T$ and a parameter ($\#N_{succ}$ is the total number of successful runs):

$$\chi = \frac{1}{N_{succ}} \sum_{j \in \{Succ\}} \frac{v\Delta t n_j}{d_j} \qquad (8)$$

where d_j is the initial distance from the plume source of trial j and n_j is the number of steps taken to the source and $\{Succ\}$ is the set of successful runs. The quantity within the sum measures the ratio of the total distance traveled to the straight-line distance to the source. This is averaged over successful trials. Thus, χ is the average ratio of successful path length to the straight-line distance to the source. We call χ the tortuosity. Finally, we attempt to find the best parameters using Latin hypercube sampling with each parameter constrained to some range. We run the parameter sampling, first over a wide range of parameters (see Tables B.6–B.8) and then, we refine the range of parameters based on histograms of the parameters that lead to a high probability of success (depending on the plume, this can be as low as 20% and as high as 75%). The histograms that are featured in the results and appendix compare the top 10% and bottom 10% of success (maximize) or top 10% and bottom 10% of tortuosity (minimize) after the second round of optimization. Correlations are obtained using the full data sets after the second round. Throughout the paper we will use the term *initial data* to mean the initial heading and spatial location in the plume.

We remark that all the simulations are done using pixels as the spatial dimension as this is the form of the data. In the three air plumes, each pixel represents 0.075 centimeters and in the water plume, 0.058 centimeters.

2.4. Choosing parameters

There are many search and follow strategies that an animal uses to locate a plume. For example, moths go in increasingly wider paths transverse to the flow direction in order to capture a plume. Other

strategies involve Levy flights and correlated random walks. Because we have set a strict condition for failure (leave the imaged domain), we have chosen initial starting locations in the interior of the imaged region (Fig. 2) so that the algorithm has some chance to move around without exiting the domain. In all the assessments of the algorithms, we choose locations randomly (using Latin hypercube sampling) from the rectangular areas shown in Fig. 2 with an initial orientation $\theta_0 \in [\pi/2, 3\pi/2]$ also chosen randomly. Thus the agent is initially oriented toward the source.

For the **bilateral algorithm**, in the air plumes, we varied

$$\{v, \sigma, \beta, l, A_w, \gamma_w, \epsilon_w\}$$

and held $C_{hill} = 0.005, C_w = 0.01$ and $\phi = 1$ constant. In Eq. (4), C_n is the average of the concentration at the two sensors. The water plume data sets cover a much greater area so that we need to give the algorithm more time to find the source and thus it takes much more time to run a series of initial conditions over a range of parameters than for the air plumes. For this reason, we only varied

$$\{v, \sigma, \beta, l, A_w, \epsilon_w\}$$

and held $C_{hill} = .01, C_w = 0.4, \gamma_w = 5$, and $\phi = 1$. The choice to hold these parameters constant was mainly for convenience and to limit the total number of parameters varied. The choice for C_{hill} was approximately the mean concentration over all the grid points. In particular, in Victor et al. (2019), we showed that the Hill nonlinearity with $C_{hill} = \bar{C}$ was nearly optimal for transforming concentrations in order to maximize information about location in the air plumes. For the bilateral algorithm, what matters is the distance between sensors, so that since l is varied, we have held ϕ constant as the distance between sensors is $2l\sin(\phi)$. Finally, we have found that the dependence on flow direction was not sensitive to γ_w as long as it is not too close to 0 and since C_w and ϵ_w are like thresholds for determining whether to bias toward upstream and downstream (see Figure 1), we have chosen to hold C_w constant.

For the **casting algorithm**, in the air plumes, we varied

$$\{v, \sigma, \gamma_c, l, \phi_{max}, A_w, \gamma_w, \epsilon_w\}$$

and for the water plumes,

$$\{v, \sigma, \gamma_c, l, \phi_{max}, A_w, \epsilon_w\}$$

and kept $\gamma_w = 5$. All the other parameters were fixed as in the previous paragraph. The ranges of the parameters in the first round of optimization were quite broad and in the second round were narrowed down to cover the ranges in the top 20%–70% success. Specific values are found in Tables B.6–B.8 in Appendix A.

For each set of parameters we chose 2000 initial conditions taken from the regions shown in Fig. 2 using Latin hypercube sampling and ran the algorithm until the agent reaches the source or leaves the domain. For successful trials we determined the total distance traveled divided by the distance from the source (χ, see Eq. (8)). Success rate and χ were averaged over the number of initial conditions for a given parameter set. We chose a wide range of values for each parameter and ran 1000–2000 parameter sets in each of the four plumes where the parameters were chosen using LHS. After this initial survey, we looked at the distribution of parameters that lead to at least 50%–70% success rate and then used this narrower range to find the optimal parameter sets. These are the sets of parameters that we analyze.

We have selected parameters that optimize the probability of success rather than minimizing tortuosity as our measure of tortuosity is predicated on there being a successful search. If we optimized for the straightest paths, it could be possible to have a series of straight paths simply because the agent was both close to and oriented toward the source, with failures to all the other initial data. This would minimize the tortuosity at the expense of having a low probability of finding the source. We obtain a large number of parameter sets that result in high success. We then sort results by both success and tortuosity to see what parameters are good for both and how the choices differ.

3. Results

3.1. Plumes and sample trajectories

We first present results from simulations of the two simple algorithms in air and water. In each of the two algorithms we look at one water plume and three air plumes. Fig. 2 shows the log of the concentrations for each of the four plumes along with the boundaries of the initial data and the scale of the sensors for the agent. The spatiotemporal structure of the four plumes are all quite distinctive owing to differences in the Reynolds number, Schmidt number, and source configuration (Table A.5). For example, the relative signal (concentration) in the water plume (top left) is sparse and not at all like a smooth gradient, even close to the source. The slowest air plume (upper right) shows a reasonable concentration gradient near the source but low odor concentration once you move more than 10 cms from the left edge. The air plume that is near the bed (lower left) looks like a stationary plume with a clear gradient. As would be expected in simple concentration-dependent algorithms, there will be high success at reaching the source with this plume. Finally, the fastest air plume (lower right) has the advantage that the concentration reaches the far end of the domain, but is still complicated in structure and far from a simple gradient.

Fig. 3 shows example trajectories from each of the two algorithms (red, bilateral and white, casting) in the four different plumes superimposed over a single frame of each plume. Each of the algorithms has the common terms, W_n (Eq. (4)) and the stochastic component, σ. Between the two algorithms, (Eqs. (5), (6)), the sensor length, l and the velocity, v are common parameters. In these example trajectories, we have kept all common parameters between the two algorithms the same. Within the algorithms, the parameters are the same for each of the trajectories in the air. In the water plume, in this instance, the bilateral trajectory is more direct while the casting trajectory makes a few loops. In the 5 cm/s air plume the trajectories are similar but here the bilateral is less direct. In the near bed air plume, trajectories are almost indistinguishable. For the 20 cm/s plume the bilateral trajectory is more tortuous. We will quantify these differences in the ensuing sections.

3.2. Bilateral algorithm

For each of the algorithms we have chosen the parameters as outlined in the methods. We started with a broad range of values and then from those that led to the highest *success*, we narrowed the range and reran the parameter search again.

Fig. 4 shows the ordered success rates of 1000 parameter sets for the water plume and 2000 sets of parameters for air plumes after the second round of optimization using the initial conditions in Fig. 2. The scattered points show the parameter χ for the corresponding sets of parameters. The bilateral algorithm with information about the flow direction can achieve about 90% success rate at the best parameters in the water plume with χ ranging between 2 and 7 for the top performers. Thus, we can achieve good success with a reasonably direct path to the source with this simple algorithm. The tortuosity χ seems to obey the same trend in parameter space, that is, better success leads to a shorter path.

To quantify the relationships between parameters, success, and tortuosity, we have computed the correlations between the two metrics and the parameters that we varied in the bilateral algorithm. Table 1 shows the correlation between success and χ for the water plume is negative which implies that as success goes up, χ is reduced; the same parameters improve both metrics. The 5 cm/s air plume has a weak positive correlation between success and χ which implies better success means more tortuosity. However the two faster air plumes have a strong negative correlation between success and tortuosity so that better success means a more direct path.

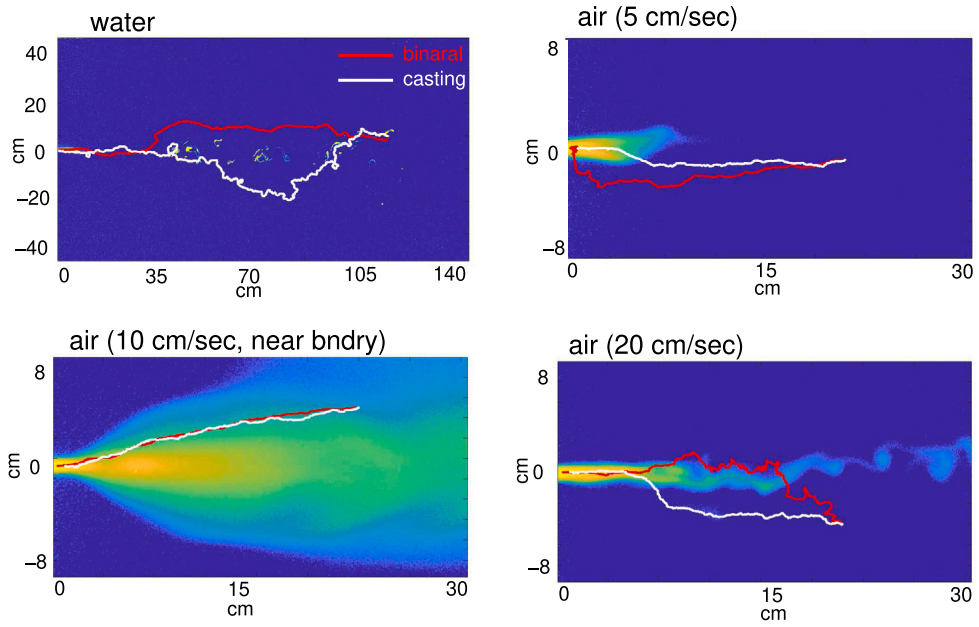

Fig. 3. Sample trajectories of the two algorithms in each of the plumes. In the case of the air plumes, all parameters are the same for each plume.

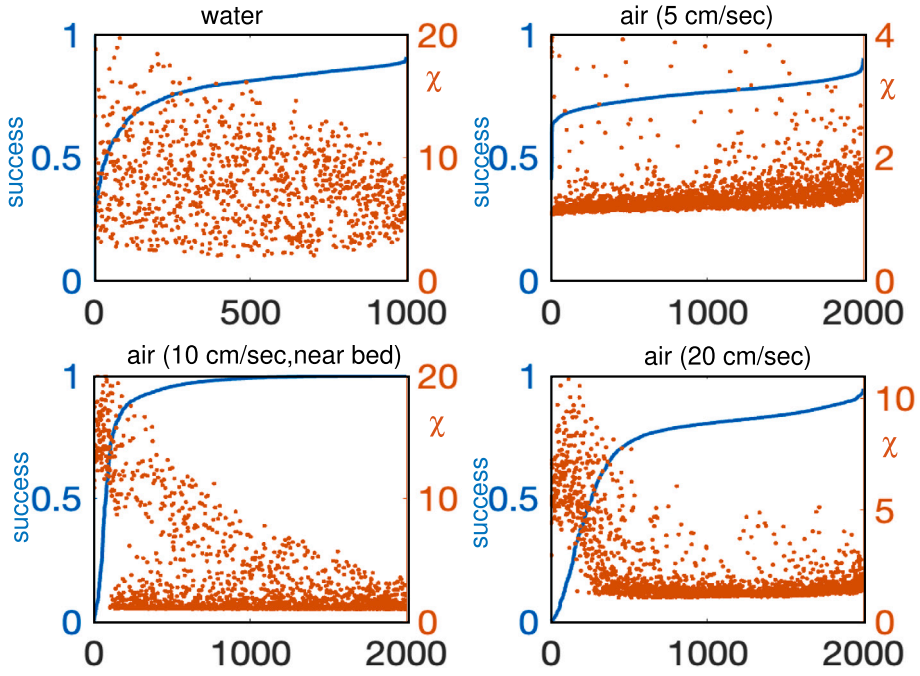

Fig. 4. Success rate and χ over a sample of bilateral parameters for each of the four plumes. Parameter sets are ordered by success rate. χ is scattered in orange while the success is in blue.

Table 1
Correlations of the varied parameters with success (S) and with tortuosity (χ) for the water (w) and the three air plumes (a5,a10,a20) using the **bilateral** algorithm. X denotes no significant correlation ($P > 0.01$) In addition, we also note the correlation between success and χ.

plume	v	σ	β	l	A_w	ϵ_w	S	χ
w(S)	−0.4589	0.2548	−0.1997	0.2000	0.2093	−0.1416	1	−0.1595
w(χ)	0.3326	0.7069	0.4030	−0.1798	−0.2368	0.1515	−0.1595	1
a5(S)	−0.2588	−0.2011	0.1798	0.3029	−0.3082	0.2798	1	0.0615
a5(χ)	−0.3180	0.2804	0.1646	0.4911	−0.2470	0.2022	0.0615	1
a10(S)	0.2208	X	−0.1618	−0.3547	X	X	1	−0.7254
a10(χ)	−0.2193	X	0.3505	0.5926	−0.0837	X	−0.7254	1
a20(S)	X	X	−0.1721	−0.5918	X	X	1	−0.7820
a20(χ)	−0.1099	0.0805	0.4086	0.6056	−0.0840	0.0876	−0.7820	1

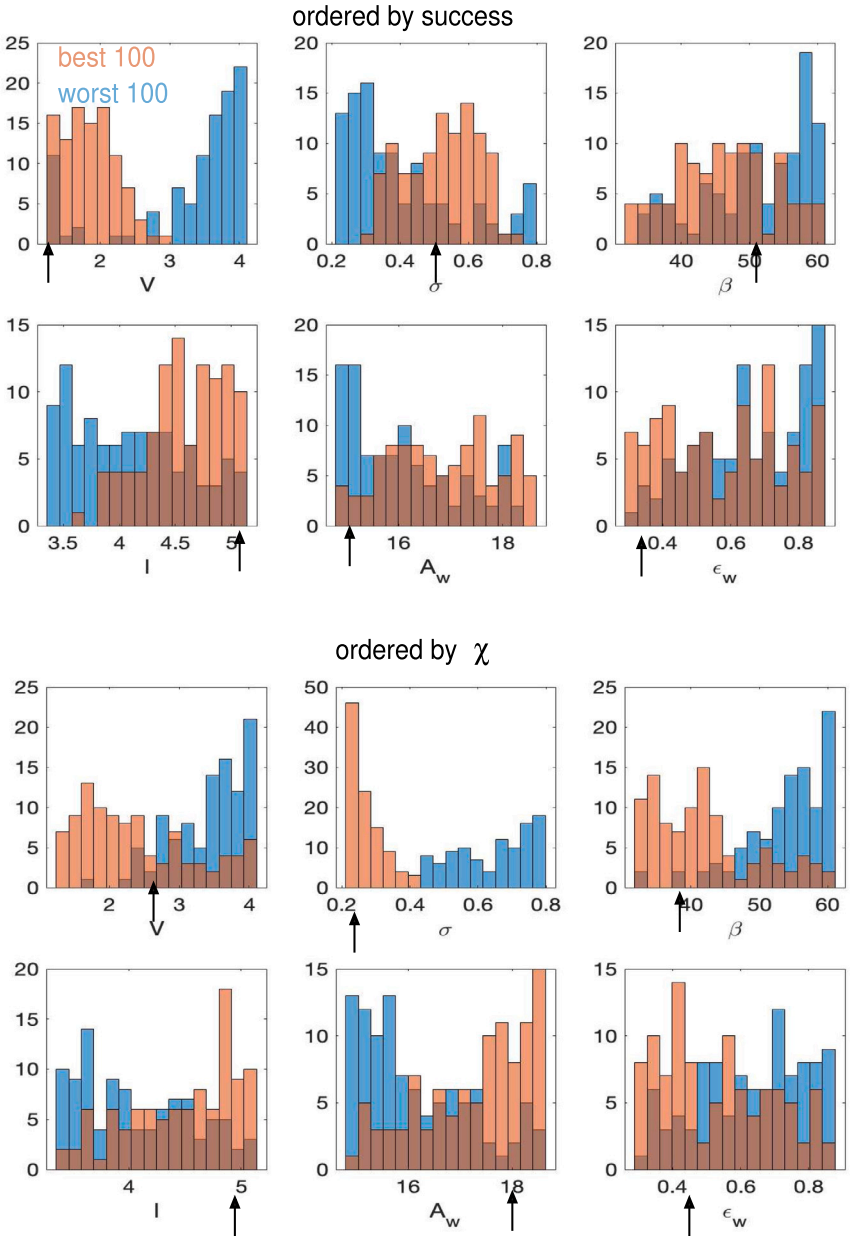

Fig. 5. Best and worst 100 parameters after the second iteration of optimizing parameters. Top: ordered by success; bottom, ordered by χ for the water plume and the bilateral algorithm. Arrows denote the best parameters for maximizing success or minimizing χ.

Table 1 also shows the correlations of $v, \sigma, \beta, l, A_w, \epsilon_w$ with the success and χ for the bilateral algorithm in each of the four plumes. Entries where $P > 0.01$ are denoted with an X. For most of the entries, $P < 10^{-4}$. As the correlation with γ_w was insignificant for the air plumes, it is not included in the table. Histograms of the parameters associated with the best and worst success and tortuosity are shown in the main text and in the appendix in Figs. 5–B.10.

3.2.1. Water plume

The results of the second round of optimization for the water plume are shown in the histograms in Fig. 5. To get these histograms, we first order the parameter sets by success. Then we create parameter distributions for the top 10% and bottom 10% success rates. Then we reorder according to χ and again take the best and worst. From this, we see that slower navigation (smaller v), more sensitivity to left–right concentration differences (larger β), less downstream movement (smaller ϵ_w), larger random search (σ), longer sensors (l) and greater sensitivity to flow direction (A_w) are compatible with higher success. Lower β, σ and higher A_w are all associated with straighter paths to the source. Indeed, there is a sharp difference in the distribution of the parameters σ, β, A_w to minimize χ. High values of β and σ lead to more turning while higher values of A_w result in more direct paths. The latter is because large values of A_w combined with sufficient odorant concentration push the agent upstream toward the source. One can think of $\beta, \sigma, \epsilon_w$ as "exploratory" as they tend to cause the agent to take longer paths and thus visit more of the domain.

In Table 2 we list the parameters which maximize success and minimize χ for the bilateral algorithm in the water plumes. The main differences are v and β. For optimal success move slowly and be sensitive to small changes in sensor differences while to get there with minimal twists and turns, move faster and be less sensitive to sensor differences. The minimal tortuosity that we attain is 1.98 and this is associated with 80% success rate. To better explore the statistical significance of the parameters associated with success, we chose 100 sets

Table 2
Optimal parameters for the bilateral algorithm with respect to success rate (S), minimum tortuosity (χ) and a weighted average ($Z = S - \chi/10$) for the four tested plumes over the parameters.

Plume	v	σ	β	l	A_w	ϵ_w	S	χ	Z
w(Z)	1.4921	0.2231	35.6274	4.9924	15.1483	0.3637	0.8425	2.0579	0.6367
w(S)	1.3199	0.4782	51.2097	5.0508	15.5188	0.3755	0.9095	5.4425	0.3653
w(χ)	2.7088	0.2289	37.5790	4.9860	18.0946	0.4640	0.8065	1.9859	0.6079
a5(Z)	0.4348	0.2337	44.6021	0.6368	5.1158	0.2905	0.9045	1.6409	0.7404
a5(S)	0.4348	0.2337	44.6021	0.6368	5.1158	0.2905	0.9045	1.6409	0.7404
a5(χ)	0.8766	0.2622	34.3926	0.5081	7.8874	0.0471	0.6365	1.0741	0.5291
a10(Z)	1.8058	0.2332	43.7649	0.5761	5.8261	0.1169	1.0000	1.0126	0.8987
a10(S)	1.7844	0.2992	31.7736	0.8559	5.7068	0.3562	1.0000	2.2803	0.7720
a10(χ)	1.8058	0.2332	43.7649	0.5761	5.8261	0.1169	1.0000	1.0126	0.8987
a20(Z)	0.5129	0.2229	40.0224	0.5346	4.4300	0.1582	0.9475	1.5761	0.7899
a20(S)	0.5129	0.2229	40.0224	0.5346	4.4300	0.1582	0.9475	1.5761	0.7899
a20(χ)	1.1515	0.4501	11.4173	0.4882	8.2746	0.0433	0.7330	1.0711	0.6259

of different random initial starting locations and orientations using the optimal parameters from Table 2. We computed the average success, S, tortuosity, χ and $Z = S - \lambda\chi$ for each set. The distribution of S, χ, Z are given in Fig. C.15 in Appendix C. They all lie in a very narrow range.

3.2.2. Air plumes

The success rates for the air plumes at the optimal parameters ranged from 100% success for the 10 cm/s plume to 90% for the 5 cm/s and 95% for the 20 cm/s air plumes. The high success rate for the 10 cm/s plume is due to the diffusive nature of the near bed flow. Despite the fact that the 5 cm/s is barely detectable at the initial starting locations (compare the three air panels in Fig. 2), there is still a high success rate. Fig. 4 shows that there is a wide range of parameters possible to maintain a reasonable success rate; there is significant fall-off in success rate only near the last 10% of the parameters for the 5 cm/s and 10 cm/s flows and success is over 70% for more than half the parameters for the 20 cm/s flow.

The three air plumes had several common features that are also close to the strategies for the water plume. (See the histograms in Figs. B.8–B.10.) Low values of υ, A_w and high values of β, ϵ_w are all associated with success. Interestingly, lower values of l are good for success in the 10 cm/s and 20 cm/s air plumes, but higher values of l are better for success in the 5 cm/s plume. We suggest that this is likely due to the limited reach of the 5 cm/s plume (c.f. Fig. 2). Bigger distances between sensors leads to greater concentration differences and thus to more turning. The optimal speeds, υ, for the 5 cm/s plume and the 20 cm/s plume are all below 1 cm/s compared to those for the 10 cm/s plume which has much larger successful velocities. Low υ, A_w and high β, ϵ_w are all compatible with more exploratory (less direct) trajectories. Recall that high values of ϵ_w lead to reversals away from the upstream direction and, thus to longer paths. In contrast, given a successful navigation, lower β, ϵ_w and higher A_w are all associated with shorter χ. These trends are quantified in the correlations in Table 1. Parameter distributions for the three air plumes are found in Figs. B.8–B.10 in Appendix A.

The best parameters for each air plume and each metric (success or tortuosity) are shown in Table 2.

3.2.3. Bilateral summary

Despite the complexity of the plumes in air and water, a simple comparison between two sensors is sufficient to access the plume and follow it to the source. For the diffusive like 10 cm/s flow, there is no tradeoff between path-length and success. The smooth plume structure requires little exploration and the plume is rarely lost, thus it is possible to make a direct path to the source as it will have the highest concentration.

The minimal tortuosity in the water plume (1.88) has 80% success while the maximal success rate of 90% has $\chi = 5.44$ so there is quite a bit more exploration needed to get that extra 10% increase in success. The main differences in parameters are υ and β; the velocity associated with the shortest average path is more than twice that of the greatest average success and β is more than 1/3 smaller when minimizing the average path length.

For the 5 cm/s flow, parameters that enhance finding the plume are all anti-correlated with those for minimizing the pathlength (Table 1). Because the "reach" of the plume is quite small (c.f. Fig. 2), exploration is much more necessary so that higher β, l, ϵ_w and lower υ, A_w provide a much greater chance of eventually accessing the plume. Because exploration is so important for this plume, this could explain why success is associated with higher tortuosity only in this plume as the other plumes all have extensive "reach". For initial conditions which are already in the basin of attraction of the plume, then increasing A_w, υ and decreasing β, l, ϵ_w provides for a more direct path.

Lastly, for the 20 cm/s flows, the only parameters that are strongly correlated with success at finding the plume are β, l. For the best parameter set, low υ, A_w give better success at finding the plumes. In contrast, higher A_w and υ leads to more direct paths.

Looking across the three air plumes, one might ask if there an optimal parameter set that gives good success in all three flow conditions. Since the range of highly successful parameters for the near bed flow (10 cm/s) is quite broad, we will focus on the parameters for the 5 cm/s and 20 cm/s. In both cases, the optimal parameters are close to each other (see arrows in the corresponding histograms), thus we choose the average of the optimal parameters, yielding $\upsilon = 0.4739$ cm/s, $\sigma = 0.2283$, $\beta = 42.31$, $l = 0.5857$ cm, $A_w = 4.773$, $log(\gamma_w) = 1.657$ and $\epsilon_w = 0.2244$. The result of running these parameters in the three plumes was 85%, 100%, and 94% success in the 5, 10, and 20 cm/s flows, respectively. Expanding the initial starting locations from $7.5 < x < 22.5$ and $|y| < 4.5$ to $3.75 < x < 12.75$ and $|y| < 6.375$ resulted in 78%, 99%, and 81% respectively for the three flows. Thus, the bilateral algorithm (among the easiest to operate in a robot or for an organism to implement with neural circuitry) can be tuned to successfully find the source of an odor in a wide range of landscapes. In the discussion, we will suggest possible neural structures that could implement the algorithm.

3.3. Casting algorithm

In order to optimize the success (S) of the casting algorithm, Eq. (6), we varied $\{\upsilon, \sigma, \gamma_c, l, \phi_{max}, A_w, \gamma_w, \epsilon_w\}$. Recall that γ_c is the sharpness parameter for the difference in concentrations between successive samples amd γ_w is the sharpness for the dependence of the flow effects on the concentration of the sensors. For the water plumes, this is held fixed, but was varied in the air plumes.

Fig. 6 shows the ordered success rates of 1000 parameter sets for the water plume and 2000 sets for each of the air plumes using initial data from the regions depicted in Fig. 2. The scattered plots are the tortuosity, χ. We can achieve 91% success rate in the water plume with a tortuosity ranging from 4 to 10 in the top 50 performers. As with the bilateral algorithm, there is a weak but significant negative correlation

Table 3
Correlations of the varied parameters with success (S) and tortuosity (χ) for the water (w) and the three air plumes (a5,a10,a20) using the **casting** algorithm. The correlation between S and χ is also shown.

plume	v	σ	γ_c	l	ϕ_{max}	A_w	ϵ_w	S	χ
w(S)	−0.3020	−0.2713	X	X	0.3180	0.1692	−0.0688	1.0000	−0.0741
w(χ)	0.1933	0.1774	X	X	0.8249	−0.3474	0.1205	−0.0741	1.0000
a5(S)	X	X	0.1173	−0.1593	0.1757	X	X	1	−0.1720
a5(χ)	−0.1345	X	0.1252	0.2953	0.2760	−0.2167	0.0877	−0.1720	1
a10(S)	X	−0.0636	0.0594	−0.7101	0.3154	X	X	1	−0.0564
a10(χ)	−0.0688	0.0456	0.1712	0.3282	0.4397	−0.2914	0.0927	−0.0564	1
a20(S)	−0.1843	X	0.2027	−0.1823	0.3641	X	X	1.0000	0.1248
a20(χ)	X	0.0263	0.1615	0.4089	0.6247	−0.4588	0.1803	0.1248	1.0000

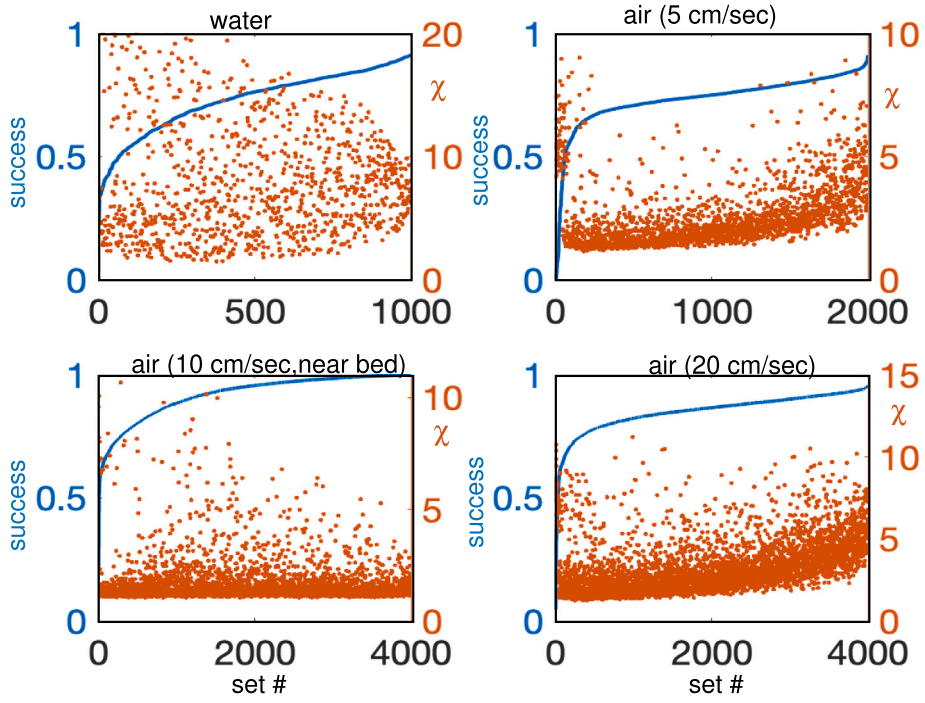

Fig. 6. Success rate and χ over a sample of casting parameters for each of the four plumes. Parameters are ordered by success rate and the corresponding values of χ are shown in orange.

between success and tortuosity (Table 3 top rows). Indeed, the general trends in water are nearly identical. The correlations between S and χ in the air plumes have opposite trends for casting and bilateral. There is a reasonably strong *negative* correlation between success and tortuosity for the 5 cm/s air plume using casting whereas there was a weak *positive* correlation using bilateral. For the 10 cm/s air plume there is a weak negative correlation between S and χ and for the 20 cm/s air plume there is a reasonable positive correlation.

Table 3 also shows the correlations between S, χ and the parameters, $v, \sigma, \gamma_c, l, \phi_{max}, A_w, \epsilon_w$ for each of the four plumes. As with the bilateral algorithm, there is no significant correlation of any of the parameters with γ_w, so it is not included in the table.

With casting, ϕ_{max} plays a role similar to β in the bilateral algorithm. Figs. B.11–B.14 in the Appendix show the distribution of parameters for maximizing success and minimizing χ for the four different plumes. We see trends similar to those in the bilateral algorithm; parameters associated with more turning are good for success and those with less turning are best for minimizing the path-length.

3.3.1. Water plume

To optimize success, it is best to maintain a low velocity (v), small noise (σ), larger ϕ_{max}, and stronger dependence on flow direction (A_w). Compared to the bilateral algorithm, the optimal velocity for casting is larger and the noise is smaller. The casting algorithm has an intrinsically stochastic term (the sampling of ϕ is random) so this may explain the smaller added noise. Since the casting depends on temporally sequential steps, having a larger velocity provides a greater spatial separation between the two samples that are compared, so this may explain the larger trend in optimal velocities. (We will see similar velocity trends in the air plumes as well.) Both v and ϕ_{max} have fairly sharp boundaries between the best and worst values. The values of l, γ_c have no significant correlation with success in the range tested. Indeed, the optimal length l tends to be between 3 and 5 cm for both algorithms. The optimal ϵ_w is quite a bit larger for casting than for the bilateral algorithm; thus when out of the plume the force to go downstream is much stronger. There is slightly more dependence on flow direction (A_w) for casting than for the bilateral algorithm. Tortuosity is minimized with smaller ϕ_{max} (smaller maximal turns), smaller σ and smaller ϵ_w (less likely to reverse trajectory) as one would intuitively expect. Parameters that maximize success or minimize tortuosity are shown in Table 4, The gain in success from 72% to 91% comes at a cost in χ going from 1.5 to 8.09 so that there is a large increase in tortuosity to gain a small percentage in success. We will address this large discrepancy below.

3.3.2. Air plumes

The maximal success rates for the air plumes ranged from 91% for the 5 cm/s to 100% and 96% for the 10 cm/s and 20 cm/s plumes

Table 4
Optimal parameters for the casting algorithm with respect to success rate (S), minimum tortuosity (χ) and a weighted average ($Z = S - \chi/10$) for the four tested plumes over the parameters.

Plume	v	σ	γ	l	ϕ_{max}	A_w	ϵ_w	S	χ	Z
w(Z)	1.8818	0.0721	2.9762	4.2812	1.3145	18.5316	0.8016	0.8310	2.1687	0.6141
w(S)	2.2630	0.1727	2.9797	4.4127	2.2262	17.3538	0.8782	0.9155	8.0893	0.1066
w(χ)	1.9351	0.0858	2.9710	3.3577	1.0381	18.5042	0.3063	0.7195	1.5000	0.5695
a5(Z)	0.4512	0.3992	2.4120	1.0710	2.0037	4.9125	0.2895	0.8427	1.9756	0.6451
a5(S)	0.8014	0.5402	2.2463	1.1858	2.7718	6.0566	0.3795	0.9127	4.3464	0.4781
a5(χ)	0.4229	0.2409	1.0843	0.8618	1.9611	7.6931	0.1527	0.6453	1.1667	0.5286
a10(Z)	0.9608	0.3324	1.7434	0.7387	1.2073	6.9309	0.2356	0.9984	1.0812	0.8903
a10(S)	0.8940	0.2119	1.4007	0.7418	2.0910	5.0481	0.1326	1.0000	1.2004	0.8800
a10(χ)	0.9273	0.2929	2.1601	1.1422	0.8504	6.7115	0.1746	0.8996	1.0543	0.7942
a20(Z)	0.5393	0.4620	2.6316	1.4138	1.8405	5.8861	0.1211	0.9024	1.8567	0.7167
a20(S)	1.2660	0.4647	2.5715	1.4437	2.6434	5.8767	0.2929	0.9584	6.7817	0.2802
a20(χ)	0.6300	0.7503	1.1372	0.8077	1.7597	7.4962	0.2018	0.7348	1.2486	0.6099

respectively. Thus, at the optimal choices, casting performs with the same success rate as does the bilateral algorithm. As with bilateral, the diffusive character of the near bed 10 cm/s flow assures that a local gradient seeking algorithm should perform well. Reasonable success can be found over a broad range of parameters (Fig. 6); the fall off over parameters is similar to that found with the bilateral algorithm (compare Fig. 4). With the 20 cm/s flow, the fall off for casting only occurs for the last 5% of the parameters. The distributions of parameters for the best and worst runs are shown in Figs. B.12-B.14. Again as in the bilateral algorithm, slow velocities are necessary but not sufficient for success. For the 5 cm/s flow, any velocity less than about 2 cm/s gives over 83% success and with the 20 cm/s flow the same range of velocities gives at least 93% success. (The top 200 scores give a range of 83%–91%, 100%, and 92%–96% success rates for 5,10, and 20 cm/s flows respectively; the bottom 200 give respectively 0%–65%, 22%–72%, and 5%–71% success.) For the 5 cm/s air plume, the only parameters that had significant correlation with success are γ_c, l, ϕ_{max} with shorter l and greater ϕ_{max} associated with success. For the 20 cm/s plume, velocity was also significantly (negatively) correlated with success. As with the bilateral algorithm, flow direction does little to help in success in the air plumes.

For all three of the air plumes, the flow direction A_w is helpful in reducing the tortuosity as it enables a more direct path to the source. Unlike with success, there is a clear delineation the A_w histograms regarding better (smaller) values of χ. Intuitively, longer sensors (l) and wider sampling angle (ϕ_{max}) are all associated with larger χ.

The optimal parameters for the three air plumes are shown in Table 4.

3.3.3. Casting summary

As with the bilateral algorithm, the casting algorithm is simple, yet it is able to both access the plume and successfully follow it to the source with high fidelity with optimal parameters. The extremely diffusive near bed 10 cm/s air plume is quite easy to navigate and there is no trade-off between success and minimizing tortuosity.

The minimal tortuosity in the water plume for casting ($\chi = 1.5$) was successful 72% of the time while the most successful set of parameters ($S = 92\%$) had $\chi = 8$, so there was a large cost to get the extra 20% success. ϕ_{max} for optimal success ($\phi_{max} = 2.22$) is more than twice the value for minimizing χ ($\phi_{max} = 1.04$). Similarly, ϵ_w is also quite a bit larger for success than for path-length ($\epsilon_w = 0.8$ for S vs 0.3 for χ). Noise σ also was different between the two optima with lower noise associated with shorter paths and less success. The other parameters are not too different. As with the bilateral algorithm, to optimize success, it is better to "turn up" the exploratory parameters (those that lead to more changes in heading), $\phi_{max}, \epsilon_w, \sigma$. However, if the plume is acquired, then reduce the exploration to shorten the path length to the source.

In the air plumes, shorter l is associated both with greater success and shorter path lengths in the casting algorithm. This result is similar to the bilateral algorithm except in the case of the 5 cm/s plume where l is positively correlated with S. Curiously, of the four plumes tested, only the 20 cm/s plume shows a positive correlation between success and tortuosity. Casting is a temporal algorithm which takes samples frame-by-frame. The higher speed plume will change more between frames, so it may be that there will be more changes in direction for casting in this plume; this leads to higher tortuosity in successful runs.

We can ask a question similar to that which we asked about the bilateral algorithm. Is there a set of parameters that works for all three flows? If we follow the prescription that was used for the bilateral and average the optimal parameters for the 5 and 20 cm/s flows, then we find that we get 95.2% success for the 20 cm/s and 88.4% success for the 5 cm/s flows using $v = 1.03$ cm/s, $\sigma = 0.5$, $\log_{10}(\gamma_c) = 2.4$, $l = 1.31$ cm, $\phi_{max} = 2.70$, $A_w = 5.95$ and $\epsilon_w = 0.320$. However, we get only 47% success for the 10 cm/s flow. Consulting the histograms in Fig. B.13, we see that these parameters all lie in the highly successful bins *except* $l = 1.31$ cm. Thus we should shorten l. Consulting Figs. B.12 and B.14, we see that shortening l should not have too large an effect on the 20 cm/s plume, but will hurt the 5 cm/s plume. We compromise and pick $l = 1$ cm and in this case obtain 85%, 98%, and 95% success rate for the 5, 10, and 20 cm/s plumes respectively. Expanding the initial conditions range (as in above), we obtain 74%, 97%, and 82% success for the three plumes. Like the simple bilateral algorithm, the casting algorithm is able to successfully find an odor source with *one set of parameters* over a wide variety of odor landscapes.

3.4. Tortuosity vs success

We have focused on two different measures of success: the probability of finding the source (S) and minimal path length (χ). Each of these has a benefit for the agent. Obviously, if the source is not found, then there is no benefit at all. On the other hand, if χ is large, then the energy cost to get to the source (as well as the time wasted) may be prohibitive. A natural question is whether there is some type of compromise between the best success ("accuracy") and the straightest path ("speed"). For example, in the 20 cm/s air plume, optimizing casting for success yields a path with $\chi = 6.78$ with 96% success and optimizing for minimal χ ($\chi = 1.03$) has success of about 73%. Thus, the price for the extra 20% success is a mean pathlength that is over fivefold longer. One possibility would be to maximize a combination, say $Z = S - \lambda\chi$. Here, λ is a parameter penalizes success, S for too much tortuosity, χ. We observe that for all the plumes, values of χ for success rates above 60% are generally between 1 and 8 and for the lowest values of χ (say below 5), the success rate is between 0.5 and 0.9. This suggests choosing $\lambda \sim 1/10$ so that the magnitudes of S and $\lambda\chi$ are close. This choice of λ is somewhat arbitrary and is used as an example. The optimization of parameters depends only on success for reasons already outlined above. Thus, one could change the value of λ to come up with "best" parameters depending on the desire to maximize success or minimize tortuosity.

In Tables 2 and 4 we list the optimal parameters for success, χ, and Z for the bilateral and casting algorithms in the four plumes. (Note that our initial round of optimization is always based on success and the scores here use the ranges from that first round of parameter searching.) For the bilateral algorithm we find a new set of parameters for water which reduces the success from 90% to 84% but at the same time more than halves the tortuosity. For the air plumes the parameters which maximize Z lead to parameters that either optimize S or χ. In contrast, for casting, there are novel sets of parameters for all four plumes. For the water plume we reduce that optimal success from 92% to 83% but also reduce χ from 8.1 to 2.2, an almost fourfold improvement. At the minimal $\chi = 1.5$ for water, $S = 72\%$. For the 5 cm/s air plume we reduce the success from 91% to 84% and halve the tortuosity. In comparison, the optimal $\chi = 1.67$ has a success of only 64%. For the 20 cm/s flow we reduce χ from 6.78 to 1.85 which only reduces success marginally from 96% to 90%. As expected, we do little to change the success and tortuosity of the near bed 10 cm/s plume as the minimum χ and optimal success have pretty similar parameters.

4. Discussion and conclusions

In this paper, we compared two simple local algorithms for using odor cues to navigate to a source in diverse environments. Our main findings can be summarized as:

- For the gradient-like near-bed plume, either algorithm is successful over a wide range of parameter choices (Figs. 4, 6);
- In general slow agent velocity gives better success rate overall, but higher velocity reduces tortuosity and leads to a more direct path;
- Increasing the parameters which affect the heading sensitivity to concentration differences (β for the bilateral algorithm and ϕ_{max} for the casting) lead to greater success rate at the expense of increased tortuosity;
- Noise in the heading increases the success rate up to a point, but leads to longer path-lengths;

It is natural to ask if the behavioral correlates of our simple algorithm are observed in animals. In fact, all three parts of our algorithms have behavioral correlates in animals. As noted in the introduction, many animals use bilateral comparisons (tropotaxis) between two sensors to follow trails and odor plumes in both air and water (Kajiura et al., 2005; Rajan et al., 2006; Catania, 2013). The bilateral algorithm is a simple implementation of this search strategy. Similarly, orienting based on successive odor samples (klinotaxis) is well-known across many species (reviewed in Martinez (2014), Baker et al. (2018)). Indeed, neural circuits for *C. elegens* have been worked out for this behavior in the nematode (Izquierdo and Beer, 2013). Thus, the core algorithms (“bilateral” and “casting”) in this study are well supported by animal behavior.

Another important part of our algorithm (particularly in the water plume) is the use of the flow direction. Our algorithm has two components: move upstream when the concentration is sufficiently large (A_w, in our model) and downstream if it is not (ϵ_w). This is a common strategy used by many organisms (Cardé and Willis, 2008; Cardé, 2021; Matheson et al., 2022) based on the fact that a odor plume typically gets wider in the downstream direction and thus, an animal is more likely to encounter it. Moths use a similar strategy in which they make wider and wider loops transverse to the flow direction (Talley et al., 2023).

Animals use a variety of search strategies to navigate in the absence of odor cues. Among the most common is the correlated random walk (Bovet and Benhamou, 1988). The parameter σ used in our model controls the magnitude of the random search.

We have not attempted to fit the parameters in any of our algorithms to specific animal search strategies. However, in an earlier papers, Liu et al. (2020), Hengenius et al. (2021) we used mouse behavior to choose parameters such as the sensor length, l, speed, v, and maximal angles for search, ϕ_{max}, to match the paths of mice seeking an odor spot.

We found that for plume a10 (air, 10 cm/s, bounded), that parameters that maximized success also lead to low tortuosity (see Tables 2 and 4 and similarly, those that minimized the tortuosity also lead to high success. This was not the case for plumes a5,a20, and w. For example, in the water plume (w), the most successful parameter set for casting (91.6%) had $\chi = 8$ and the parameter set minimizing χ had a success rate of only 71%. The concentration in plume a10, is quite smooth in time and in space, so that the algorithms have little trouble keeping on a path to the source. Indeed, both algorithms are essentially gradient climbers and plume a10 is the most gradient like of the tested plumes. In the other plumes, a5,a10, and w, the algorithms are more likely to lose the plume. If the plume is lost, then parameters that increase the tortuosity will increase the chance that the agent will capture the plume before it exits the domain. One could view this as a ”speed-accuracy” trade-off; successful strategies need to avoid straight paths to the border of the domain if they have lost the plume. If we change the ”boundary conditions”, say, to allow the agent to ”bounce” off, then the path to the source will still be quite long, when the plume is lost as the agent must travel to an edge and then turn back. Thus, it plumes where the concentration is intermittent, parameter sets that encourage frequent direction changes will be more successful.

Despite the differences in a5, a10, and a20, for both the bilateral and casting algorithms, we found that there were parameters which led to successful navigation in all three air plumes, thus, it is not necessary to change the strategy when the odor landscape changes. By weighting the success and tortuosity (Z), we found parameter sets that had nearly optimal success and also small tortuosity (c.f. Tables 2 and 4).

In the water plume, for either algorithm, flow direction was quite important for success. Without any directionality cues, the rate of success was less than 10% (not shown here in the paper). Direction cues were less important for air plumes, mostly for reducing χ (See Tables 1 and 3). In the bilateral algorithm, in a5 plume, the correlation was actually negative between A_w (the strength of the direction cue) and S. The mechanism for this is that, if the agent is near the source in the streamwise direction, but away from it in the cross-stream, the directional cues drive the agent off the right edge of the domain.

Dynamic strategies. All of algorithms kept the parameters fixed for each trial, but it is known that animals change their strategies when they are far from the odor source. For example Liu et al. (2020) show that far from an odor spot, mice cast more widely and then tend to reduce the casting amplitude as they approach the source. This suggests that we might be able to improve success with a dynamic strategy. That is, near the plume one could use one set of parameters, but away from the plume another. This leads to the obvious question of how to tell if we are near or far from the plume. Our flow component of the algorithm, is in a sense, a dynamic strategy where we use the concentration as a surrogate for whether we are in the plume or not. A_w, ϵ_w only act when the concentration falls within some range. Other cues of plume proximity are the times between encounters; as the source is neared, the encounters become more frequent. As an example of such a dynamic strategy, we could vary the distance between sensors (either by changing l or ϕ the angle between them or ϕ_{max} in the case of casting). Insects actively change their antennae in order to better acquire and stay on the plume and mice sniff faster when they detect an odor (Wachowiak, 2011; Reddy et al., 2022; Crimaldi et al., 2022). Another clear parameter that would be good for modulation is the speed of motion, v. High speeds are good for covering a lot of area when the plume has not been located, but once locked into the plume, it is better to move somewhat slowly to avoid overshooting. Thus, a direction for further exploration would be to include some concentration dependence on, say, the velocity, ϕ or ϕ_{max}. For example, when the concentration is low, it might be better to move faster and make more turns in order to increase the probability of encountering the plume. Then once the odor is detected, slow down and turn less.

Sampling rates. Here we have sampled at every frame in the plume data which is reasonable for bilateral, an inherently continuous time algorithm. But, for casting, the discrete nature of the algorithm would realistically impose some physical limits on the rate of motion of the sensor. This would not be an issue with a robot, but mice and other animals that use klinotaxis (serial sampling), can only move at some finite speed. Thus, it would be interesting to reduce the sampling rate and see how this affects the algorithms. On the other hand, our agents have a fixed speed and thus must always move. A fairer strategy for these simple algorithms is to stop and sample, make a decision, and then move forward at a fixed rate. Choices such as how often to sample and how far to move between samples are beyond the present study.

Biological plausibility of the algorithms. Finally, we have advocated for the utility of these algorithms because they are simple to implement. Thus, a natural question is: are there plausible neural substrates for these algorithms? Jones and Urban (2018) suggest that the accessory olfactory nucleus (AON) is a possible site for the integration of the left and right naris inputs. Indeed, Kikuta et al. (2010) found neurons in the AON that respond differentially to ipsilateral and contralateral inputs. More recently, Rabell et al. (2017) found that AON neurons and cross hemispheric connections are necessary for rapid source localization by mice. Mechanistic models for deciding the larger of two stimuli include the well know winner-take-all architecture such as in models for binocular rivalry (Shpiro et al., 2007). Such algorithms can amplify small left right differences so that they could possibly improve on the simple difference that is used in this paper. We remark that in Hengenius et al. (2021), we used $(C_L - C_R)/((C_L + C_R)/2)$ as the driving force for bilateral turning; division by the mean concentration provides a contrast enhancement that is not in our algorithm. In this paper, we put our odors through a Hill nonlinearity which greatly enhances small concentrations. It would be interesting to compare which of these performs better.

Temporal comparisons (as used in the casting algorithm) require some sort of memory in order to compare changes in the odor concentration on a moment-by-moment basis. Neurons in the fly olfactory lobe are sensitive to rapid temporal changes in their inputs (“on” and “off” neurons) (Álvarez-Salvado et al., 2018), so that these could serve as substrates for making decisions about when one is moving up an odor gradient. Similarly, Parabucki et al. (2019) have shown that there are neurons in the olfactory bulb of mice that are sensitive to temporal changes on odor concentration. Thus, it seems that at least in short time scales it is possible to find neural substrates for deciding differences in concentrations when sampled at different times. Over longer time scales, in animals like mice, working memory may be necessary and in this case, a model such as in Machens et al. (2005) would suffice.

In conclusion, we have demonstrated that even simple gradient detection algorithms using spatial comparisons (tropotaxis, bilateral) and temporal comparisons (klinotaxis, casting) can be optimized so that they are able to locate odor sources in complex and diverse odor landscapes in air and water. Unlike global algorithms which require a spatial map of the world, e.g. Vergassola et al. (2007), these types of algorithms could be realized in the simplest organisms. There is strong evidence that many animals use stereo cues and casting strategies for trail and plume following. This study confirms that they can be tuned to be successful in a range of dynamic odor landscapes.

Funding

This work was funded by the National Science Foundation, United States (DBI 2014217).

CRediT authorship contribution statement

Bowei Ouyang: Writing – review & editing, Writing – original draft, Visualization, Validation, Software, Investigation, Formal analysis, Conceptualization. **Aaron C. True:** Writing – review & editing, Data curation. **John P. Crimaldi:** Writing – review & editing, Funding acquisition, Data curation, Conceptualization. **Bard Ermentrout:** Writing – review & editing, Validation, Supervision, Software, Funding acquisition, Conceptualization.

Declaration of competing interest

The authors declare that they have no known competing financial interests or personal relationships that could have appeared to influence the work reported in this paper.

Appendix A. Plume imaging details

A.1. Planar laser-induced fluorescence

Planar laser-induced fluorescence (PLIF) was used to quantify odor concentration fields by imaging the instantaneous fluorescence signal of fluorophore-dosed plumes under excitation from focused laser sheets (Fig. A.7). A passive scalar (odor surrogate) was released from a source and was transported and mixed by the ambient flow. The imaged fluorescence intensities were linearly proportional to the excitation intensity (laser power or pulse energy) and scalar concentration. Time histories of raw two-dimensional fluorescence images I_N were acquired and corrected to quantitatively map pixel intensities to relative (source-normalized) concentration levels C/C_0 based on the following algorithm adapted from Crimaldi (2008):

$$\frac{C}{C_0} = \frac{1}{a_c}\frac{I_N - b}{B - b}. \tag{A.1}$$

Here, b is the contribution to I_N from the combined dark response and background illumination present during the experiments. B is the flatfield image which maps spatial variations in light sheet (excitation) intensity and other non-uniformities due to lens vignette and pixel-to-pixel gain variations. Normalization by $B - b$ then quantitatively corrects for systematic errors owing to several experimental factors that produce nonphysical artifacts in the spatiotemporal structure of the imaged plume fluorescence field. Both b and B are obtained by averaging several hundred images of the test section in the appropriate configuration: absent any fluorescence signal but with all other illumination sources present (b) and with a constant and uniform fluorophore concentration field (B). Finally, the calibration coefficient, a_c, was used to normalize concentrations (pixel intensity) based on the source concentration at the release point.

While the core PLIF approach used for measuring the air and water plume datasets was broadly similar, notable differences in fluorophore properties in gaseous (Lozano et al., 1992) versus aqueous (Crimaldi, 2008) contexts require different excitation sources and imaging configurations. These specificities produced characteristic random (non-systematic) errors which set the effective noise floor of the measured plumes. The primary noise contribution in the air plume datasets, which were significantly signal-limited relative to the water plume datasets, came from shot-to-shot variations in laser pulse energy. For the water plumes, the dominant noise contribution came from laser light reflected by sub-micron dust particles in the flow which was not blocked by the camera filter owing to the high angles of light incidence necessary in the constrained imaging configuration. For both datasets, the estimated noise floor in the final postprocessed datasets was below 1% of the source concentration throughout the FOV. We briefly summarize other keys aspects of the experimental methods below for the air and water plumes, including descriptions of the flow facility and ambient flow conditions, odor source configurations, and the PLIF system.

Table A.5
Summary of experimental configurations and parameters for testbed air and water plume datasets.

Flow and odor release conditions

Identifier	Mean flow speed (cm/s)	Source location, release	Source diameter (cm)	Source flow rate (cm/s)
a5: freestream isokinetic, low speed (air)	5	free-stream, isokinetic	0.953	5
a20: freestream isokinetic, high speed (air)	20	free-stream, isokinetic	0.953	20
a10: nearbed isokinetic (air)	10	near-bed, isokinetic	0.953	10
w: freestream isokinetic (water)	5	free-stream, isokinetic	0.69	5

PLIF imaging

Identifier	Field-of-view (cm × cm)	Spatial resolution (mm/px)	Temporal resolution (ms)
a5: freestream isokinetic, low speed (air)	16 × 30	0.74	66.67
a20: freestream isokinetic, high speed (air)	16 × 30	0.74	66.67
a10: nearbed isokinetic (air)	16 × 30	0.74	66.67
w: freestream isokinetic (water)	80 × 146	0.586	22.22

Dimensionless parameters

Identifier	Hydraulic diameter Re	Mesh Re	Source Re	Sc
a5: freestream isokinetic, low speed (air)	996	84	32	1.4
a20: freestream isokinetic, high speed (air)	3984	337	127	1.4
a10: nearbed isokinetic (air)	1992	169	63	1.4
w: freestream isokinetic (water)	40 399	N/A	344	2400

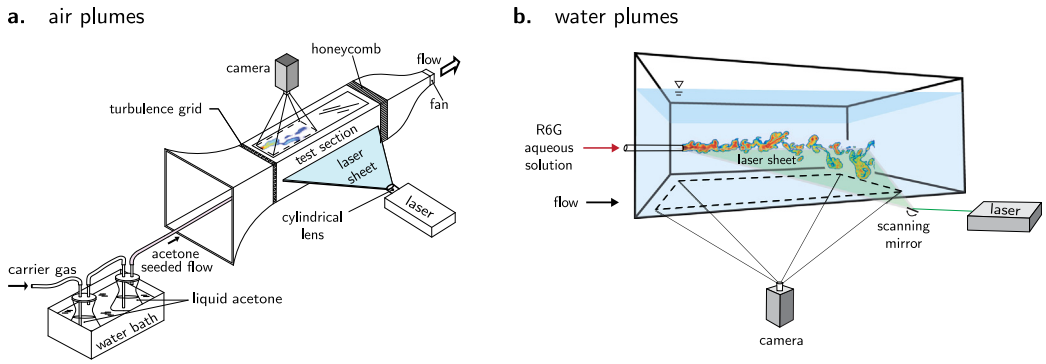

Fig. A.7. Experimental configurations used for PLIF measurements of air (**a.**) and water (**b.**) plumes.

A.2. Air plumes

Air plume datasets were measured using PLIF in a benchtop low-speed wind tunnel (see Fig. A.7a) as described in Connor et al. (2018) by releasing a fluorescent surrogate odor (a neutrally buoyant blend of saturated acetone vapor) into turbulent flow environments. The tunnel test section was 1 m long, by 0.3 m tall, by 0.3 m wide and featured a turbulence grid (6.4 mm diameter rods, 25.4 mm mesh spacing) at the upstream entrance to the test section. Flow was drawn through an inlet contraction, across the grid, and through a honeycomb conditioner at the downstream end of the test section by a suction fan that was used to vary mean flow speeds. The acetone plumes were released isokinetically through a 9.5 mm diameter tube on the tunnel centerline 10 cm downstream of the turbulence grid. A 1 mm thick light sheet was created using beam shaping optics and a cylindrical diverging lens with a Nd:YAG pulsed laser (266 nm, 70 mJ/image, 15 Hz). The excited fluorescence signal of the illuminated plume was imaged using a synchronized high quantum efficiency sCMOS camera with a notch filter to block residual green light from lower harmonic outputs of the laser. Raw fluorescence images were corrected according to Eq. (A.1) yielding time-stacks of source-normalized odor concentration fields.

A.3. Water plumes

Water plume datasets were measured using PLIF in an open channel flume as described in Ritsch (2019) by releasing a fluorescent surrogate odor (an aqueous solution of Rhodamine 6G, R6G) into a turbulent flow environment. (See Fig. A.7b.) The overall flume length was 9 m and the imaging test section was the single, central bay measuring 1.5 m long, by 0.4 m tall, by 1.25 m wide. Flow was driven in a closed-loop by a pair of pumps with variable frequency drivers from a downstream receiving reservoir into an upstream head box, then through a series of flow conditioners (gradual contraction transitioning to the flume cross-section, honeycomb) into the main flume section. A sharp-crested weir downstream was used to control the free surface elevation for a given discharge (volumetric flowrate). The flow depth was approximately 40 cm, and the R6G plumes were released on the flow cross-section centerline. A 1 mm thick light sheet from a CW laser (532 nm, 50 W maximum) was created by sweeping the beam across the imaging FOV using a scanning mirror (one sweep per image). The excited fluorescence signal of the illuminated plume was imaged using an sCMOS camera with a high-pass filter to block the green light. Raw fluorescence images were corrected according to Eq. (A.1) yielding time-stacks of source-normalized odor concentration fields.

Table B.6
Ranges of the varied parameters for the first and second rounds of optimization for the water plume for both the bilateral and casting algorithms.

Bilateral						
	v (cm/s)	σ	β	l (cm)	A_w	ϵ_w
First round	0.293 7.032	0 4	5 100	0.293 5.86	0 20	0 4
Second round	1.2306 4.1606	0.2 0.8	31 62	3.3402 5.1568	14 19	0.2 0.9

Casting							
	v (cm/s)	σ	$\log(\gamma, \epsilon)$	l (cm)	A_w	ϵ_w	ϕ_{max}
First round	0.293 7.032	0 4	4.6052 6.9078	0.293 5.86	0 20	0 4	0 3.1415
Second round	1.758 5.274	0.7 1.7	4.0943 6.8977	2.673 4.981	11 19	0 1	1 2.5

Table B.7
Ranges of the varied parameters for the first and second rounds of optimization for the three air plumes for the bilateral algorithm.

	v (cm/s)	σ	β	l (cm)	A_w	$\log(\gamma_w)$	ϵ_w
First round	0.375 4.875	0 1	1 60	0.375 2.625	0 10	0 3	0 0.5
Second round							
5 cm/s	0.375 1.125	0 0.8	35 60	0.45 0.75	3 9	0.3 1.1	0.072 0.31
10 cm/s	1.125 3.975	0.1 0.6	14.75 46.3	0.45 1.125	2.9 8.2	0.71 2.42	0.1 0.4
20 cm/s	0.45 2.25	0 0.6	7 40	0.375 1.125	4 10	0 1.5	0.05 0.25

Table B.8
Ranges of the varied parameters for the first and second rounds of optimization for the three air plumes for the casting algorithm.

	v (cm/s)	σ	$\log(\gamma_c)$	l (cm)	ϕ_{max}	A_w	$\log(\gamma_w)$	ϵ_w
First round	0.375 3.375	0 1	0 3	0.375 2.625	0.5 3	0 10	0 3	0 0.5
Second round								
5 cm/s	0.675 2.775	0.18 0.75	1.06 2.52	0.7245 1.4775	0.89 1.39	3.22 8.2	0.83 2.45	0.09 0.37
10 cm/s	0.8025 3.1725	0.18 0.75	0.97 2.54	0.642 1.464	0.83 2.25	2.71 8.15	0.63 2.39	0.1 0.39
20 cm/s	0.45525 2.175	0.21 0.78	1.03 2.57	0.71025 1.69875	1.51 2.73	2.82 8.18	0.67 2.35	0.1 0.39

Appendix B. Algorithm performance details

Parameters were chosen from broad ranges for the first round of optimization. Starting ranges for air plumes and water plumes were different due mostly to the difference in domain size. (See Tables B.6, B.7, B.8). From these, the parameter ranges were narrowed down by choosing the top 30% success rates. For each of the air plumes and the water plume, we chose different ranges in order to give the highest success per plume. These values are also shown in the tables. We then ran the algorithms on each plume using these parameter ranges and from these looked at the distribution of parameter values in the top and bottom 200 for maximizing success or minimizing χ for the three air plumes. A similar analysis is done for the top and bottom 100 for the water plume.

There are four figures for the bilateral algorithm and four for the casting algorithm. Each figure is for a different plume and divided into two parts. The top set of histograms considers the success rate and the bottom set the tortuosity, χ. For the water plume and the bilateral (casting) model, histograms are for parameters: $v, \sigma, \beta, l, A_w, \epsilon_w$ ($v, \sigma, \gamma_c, l, \phi_{max}, A_w, \epsilon_w$, respectively). For the air plumes and bilateral (casting) model, the histograms are for parameters: $v, \sigma, \beta, l, A_w, \gamma_w, \epsilon_w$ ($v, \sigma, \gamma_c, l, \phi_{max}, A_w, \gamma_w, \epsilon_w$, respectively). Note that γ_c, γ_w are presented in $\log_{10}$ units. A summary of our interpretation of these histograms is given in the main text.

Appendix C. Distribution of success and χ in water plumes

Using the optimal parameters taken from Tables 2 and 4 for the water plume, we generated 100 different sets of initial conditions to check the sensitivity of our parameter choices to the particular initial data. Figs. C.15, C.16 show that these measures all lie within a very narrow range of values so that the parameters that we have chosen for the algorithms are optimal independent of the initial data used to select them.

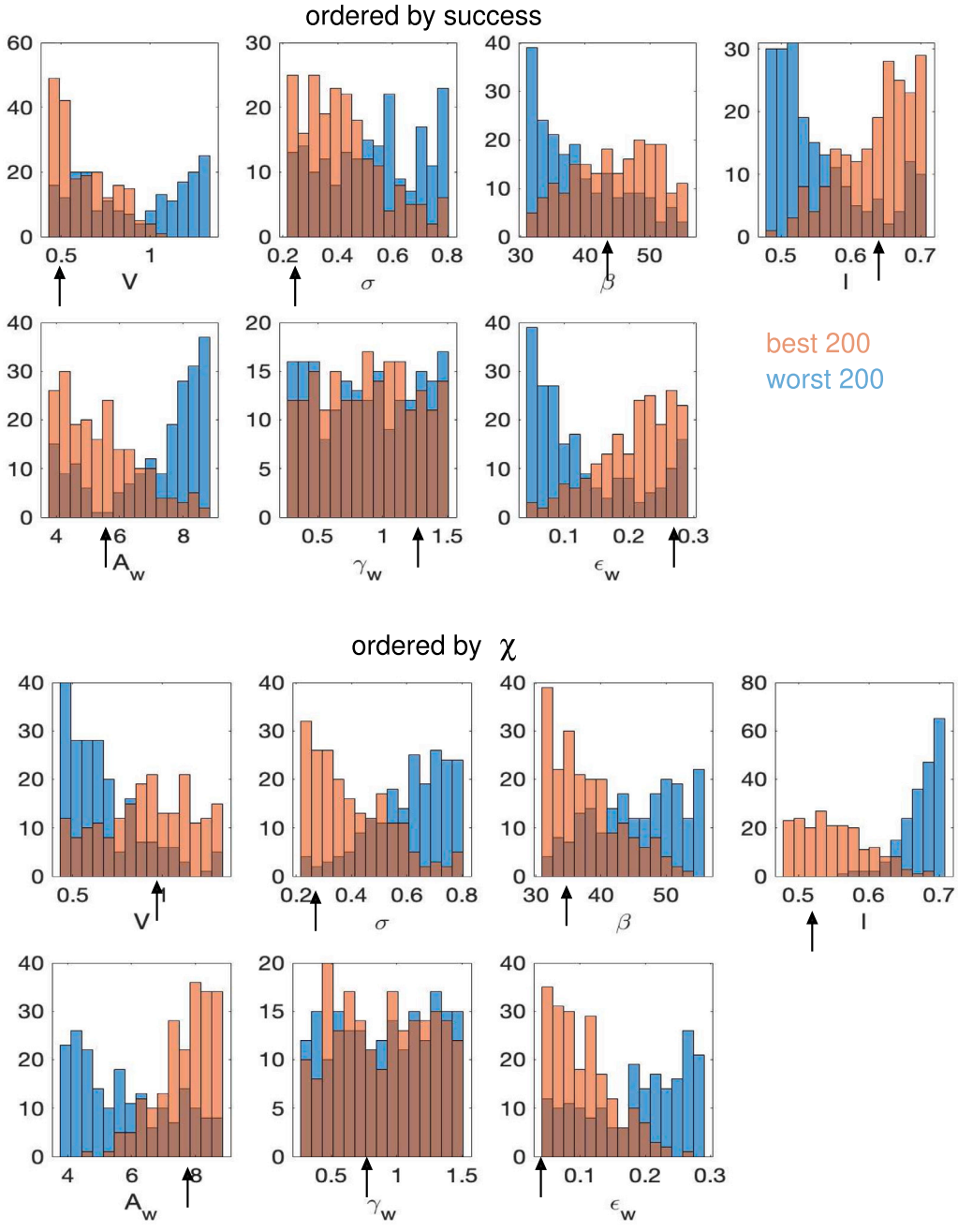

Fig. B.8. Best and worst 200 parameters after the second iteration of optimizing parameters ordered by success (top) and by χ (bottom) for the air plume (5 cm/s) and the bilateral algorithm. (Note that γ_w is in $\log_{10}$ units.).

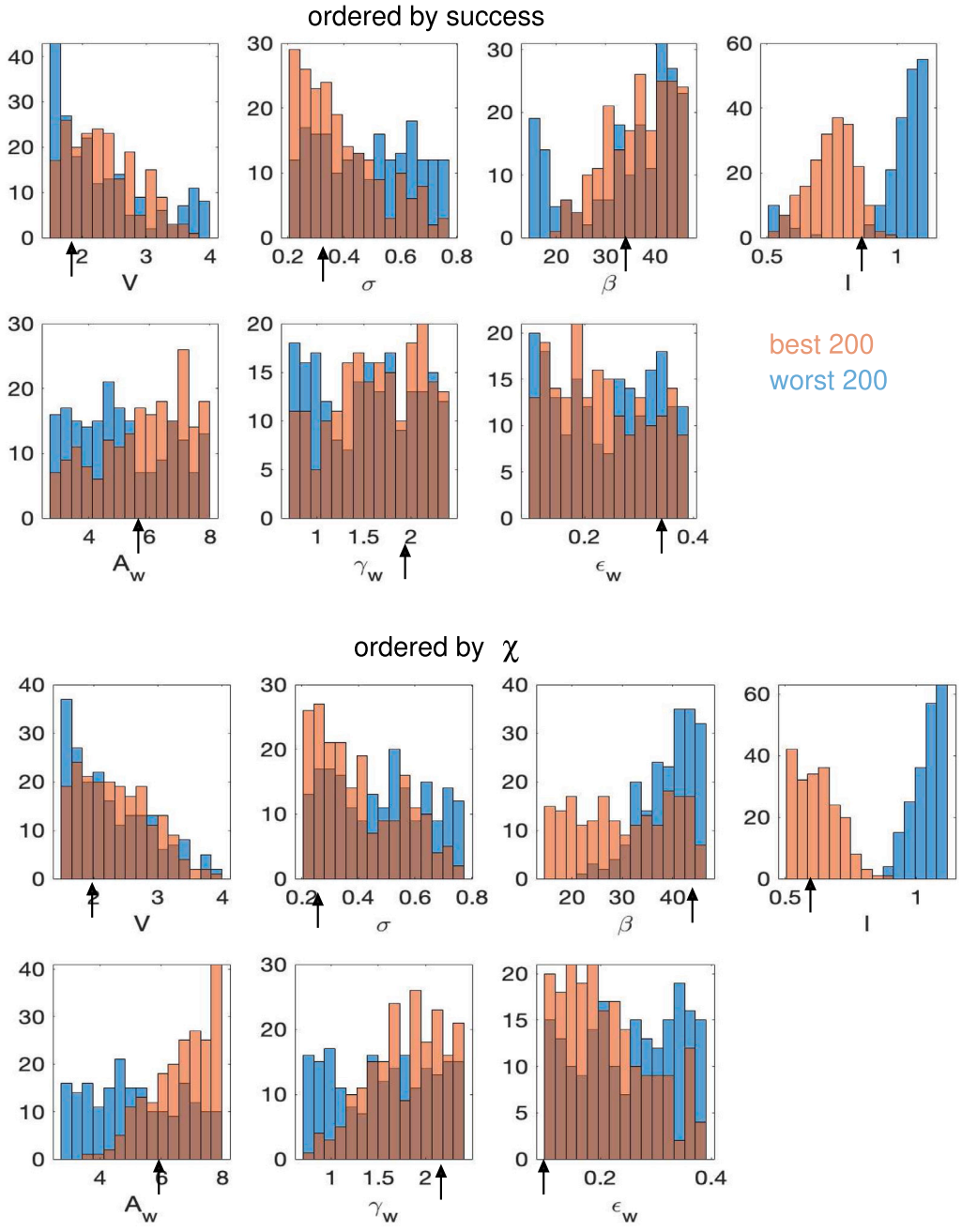

Fig. B.9. Best and worst 200 parameters after the second iteration of optimizing parameters ordered by success and by χ for the air plume (10 cm/s) and the bilateral algorithm. (Note that γ_w is in $\log_{10}$ units.).

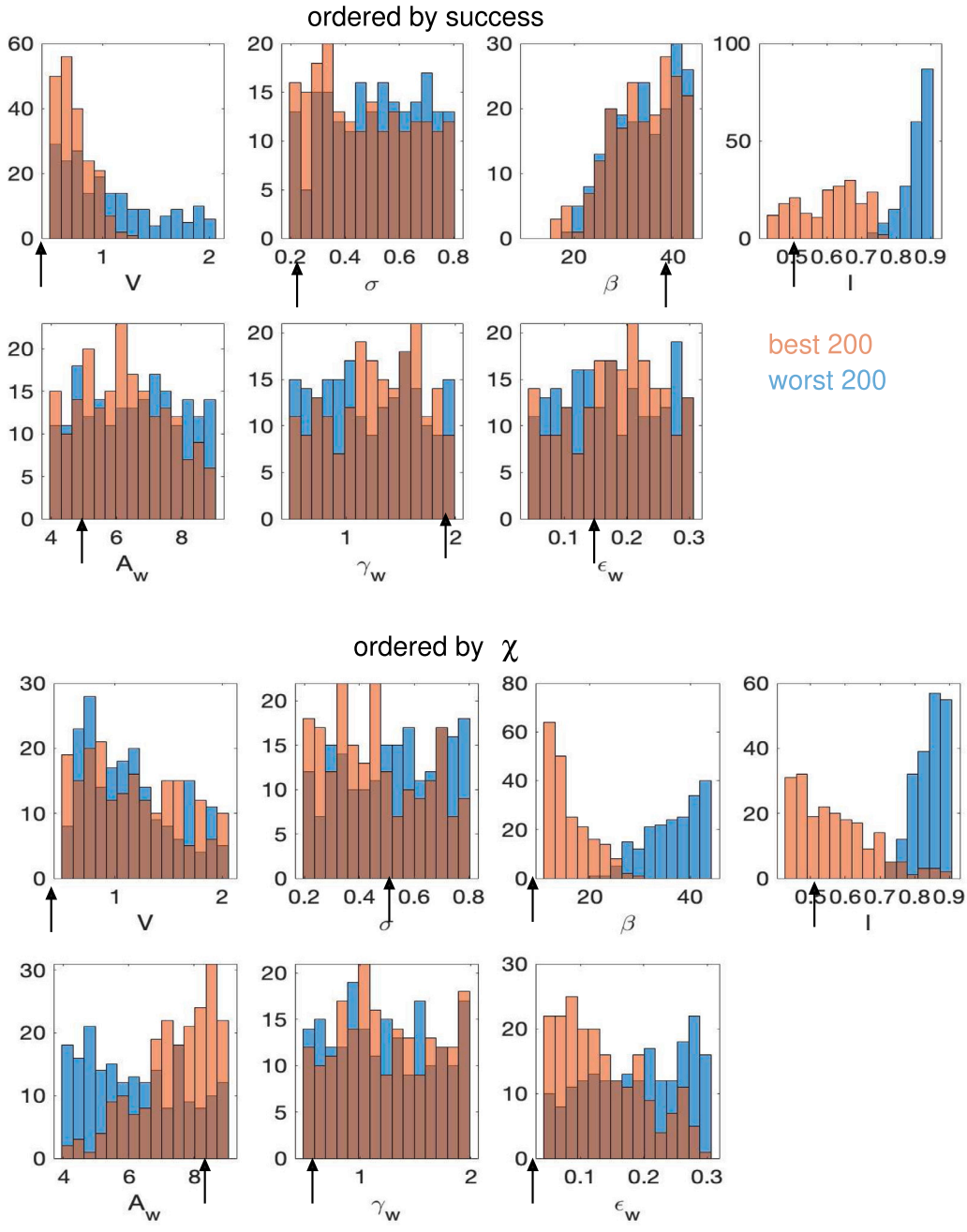

Fig. B.10. Best and worst 200 parameters after the second iteration of optimizing parameters ordered by success and by χ for the air plume (20 cm/s) and the bilateral algorithm. (Note that γ_w is in $\log_{10}$ units.).

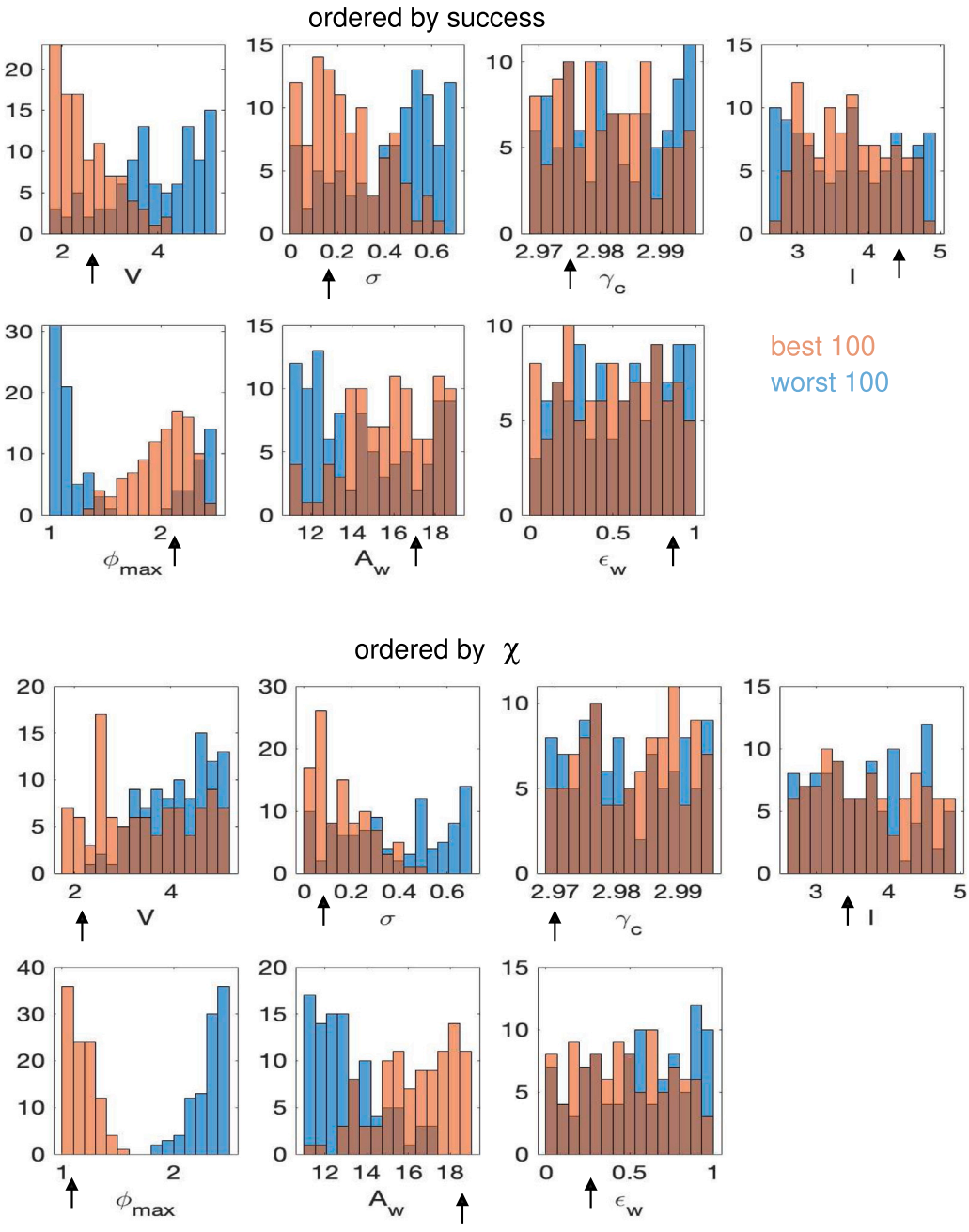

Fig. B.11. Best and worst 100 parameters after the second iteration of optimizing parameters ordered by success and by χ for the water plume and the casting algorithm. (Note that γ_c is in $\log_{10}$ units.).

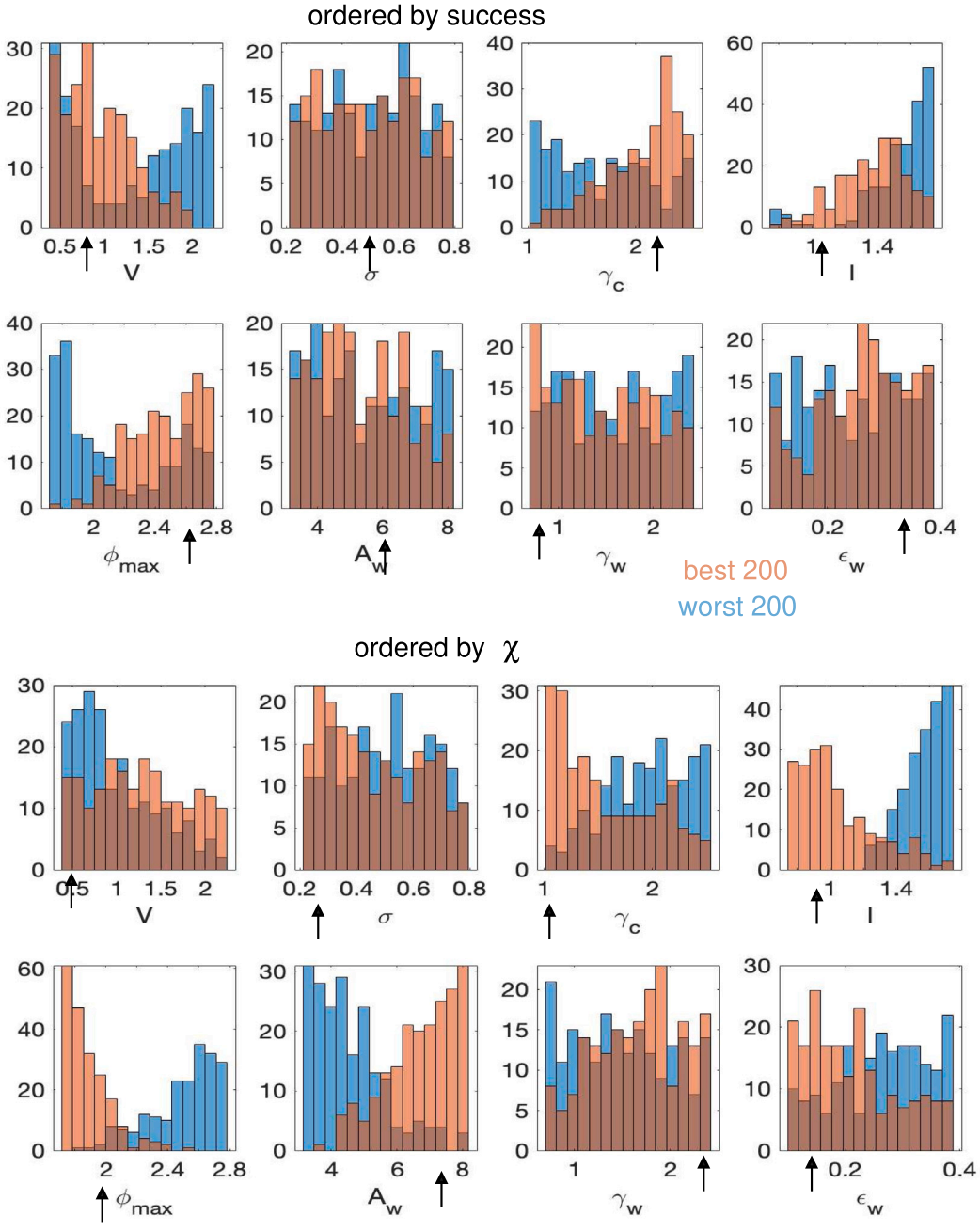

Fig. B.12. Best and worst 200 parameters after the second iteration of optimizing parameters ordered by success and by χ for the air plume (5 cm/s) and the casting algorithm.(Note that γ_w, γ_c are in $\log_{10}$ units.).

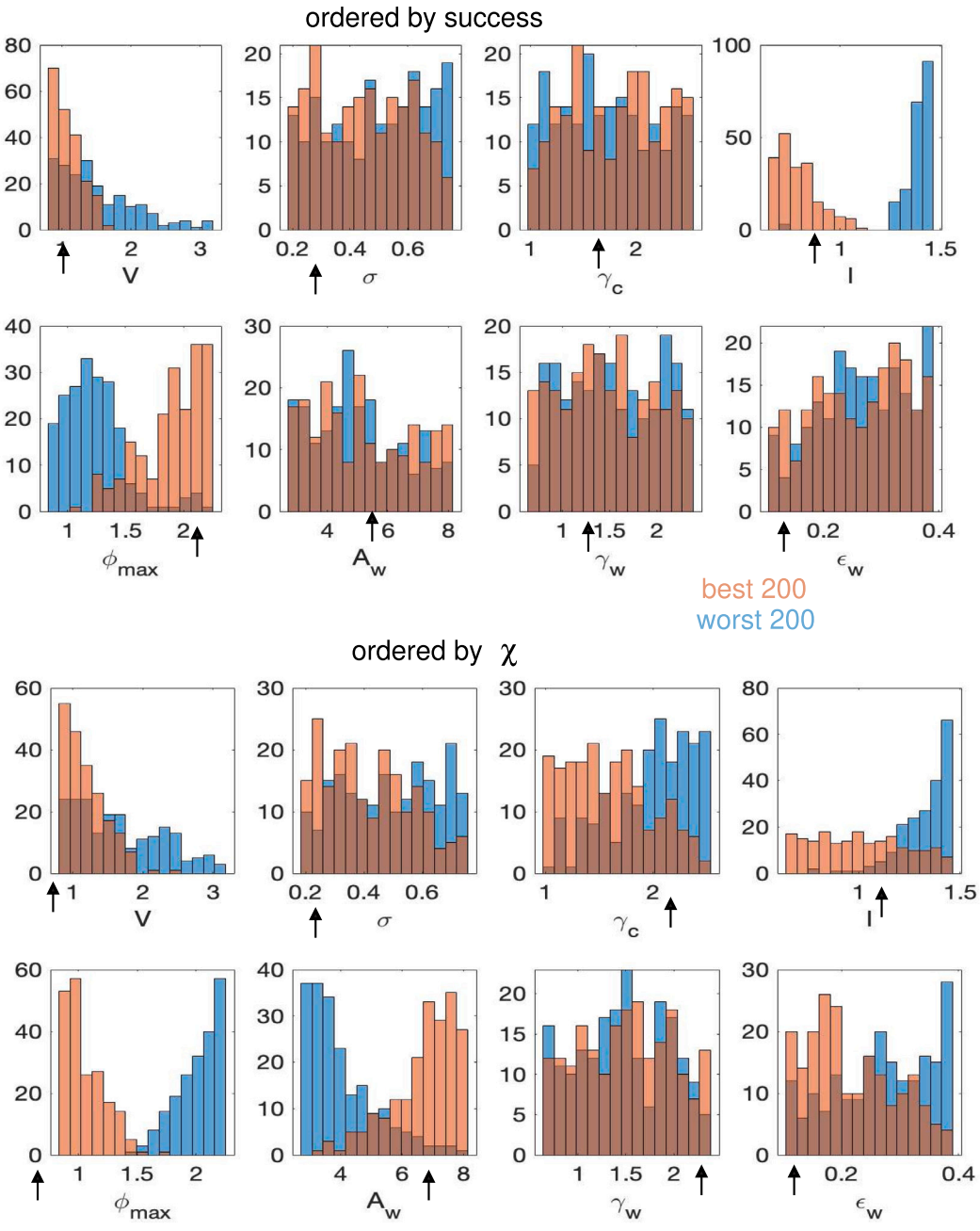

Fig. B.13. Best and worst 200 parameters after the second iteration of optimizing parameters ordered by success and by χ for the air plume (10 cm/s) and the casting algorithm.(Note that γ_w, γ_c are in $\log_{10}$ units.).

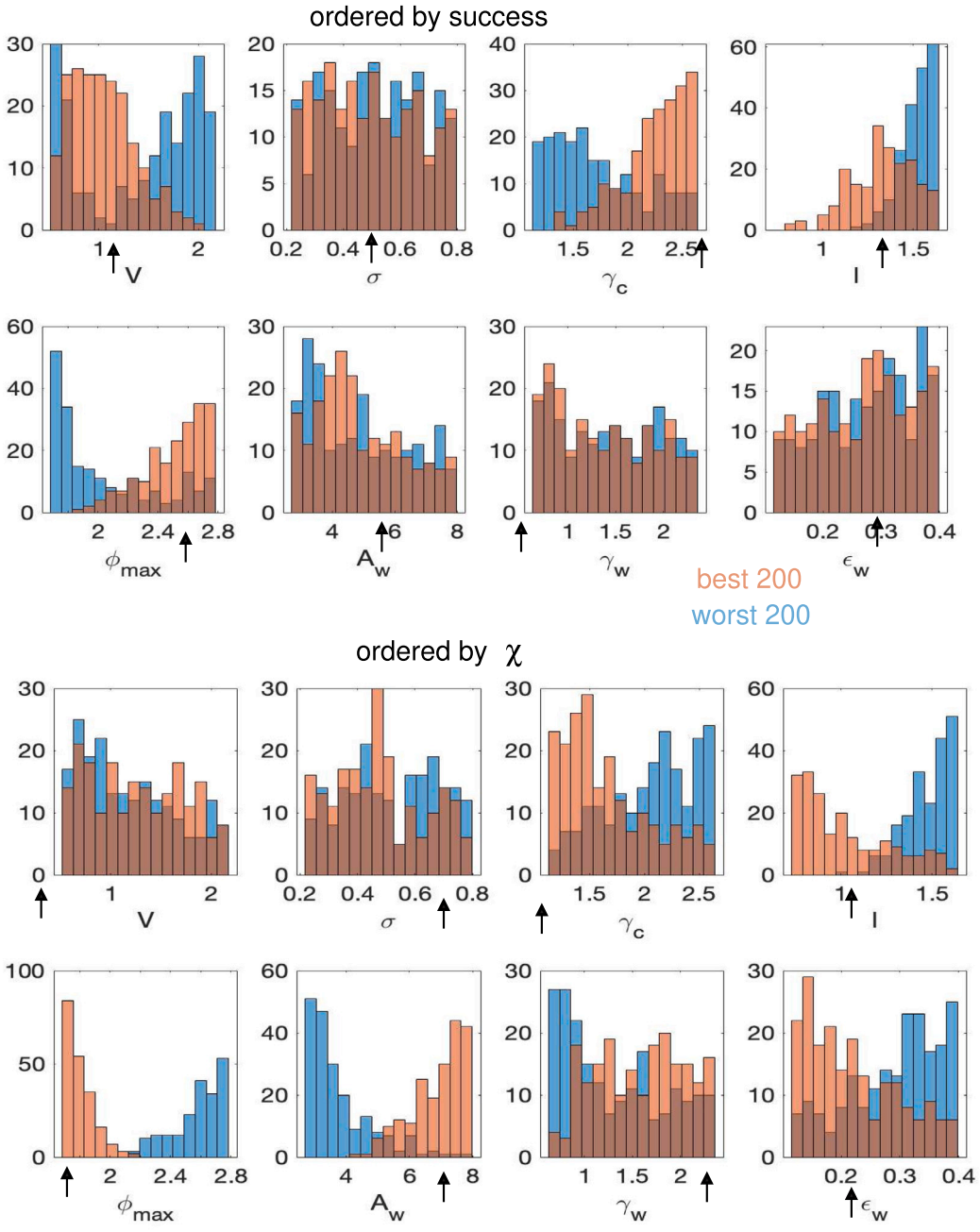

Fig. B.14. Best and worst 200 parameters after the second iteration of optimizing parameters ordered by success and by χ for the air plume (20 cm/s) and the casting algorithm.(Note that γ_w, γ_c are in $\log_{10}$ units.).

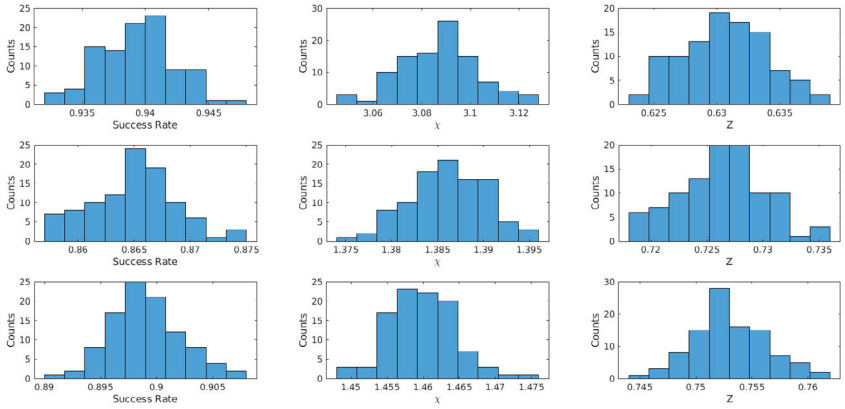

Fig. C.15. Distribution of success rates, χ, and Z for 100 sets of initial data for the optimal parameters in the bilateral algorithm. Top row: using optimal success; middle row: optimal χ; bottom row: optimal Z.

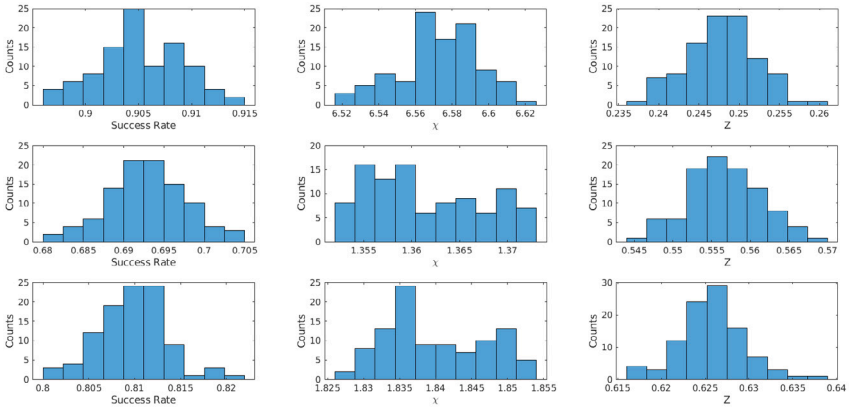

Fig. C.16. Distribution of success rates, χ, and Z for 100 sets of initial data for the optimal parameters in the casting algorithm. Top row: using optimal success; middle row: optimal χ; bottom row: optimal Z.

References

Abraham, Nixon M., Vincis, Roberto, Lagier, Samuel, Rodriguez, Ivan, Carleton, Alan, 2014. Long term functional plasticity of sensory inputs mediated by olfactory learning. Elife 3, e02109.

Álvarez-Salvado, Efrén, Licata, Angela M., Connor, Erin G., McHugh, Margaret K., King, Benjamin M.N., Stavropoulos, Nicholas, Victor, Jonathan D., Crimaldi, John P., Nagel, Katherine I., 2018. Elementary sensory-motor transformations underlying olfactory navigation in walking fruit-flies. Elife 7, e37815.

Baker, Keeley L., Dickinson, Michael, Findley, Teresa M., Gire, David H., Louis, Matthieu, Suver, Marie P., Verhagen, Justus V., Nagel, Katherine I., Smear, Matthew C., 2018. Algorithms for olfactory search across species. J. Neurosci. 38 (44), 9383–9389.

Bhattacharyya, Urvashi, Bhalla, Upinder Singh, 2015. Robust and rapid air-borne odor tracking without casting. Eneuro 2 (6).

Boie, Sebastian D., Connor, Erin G., McHugh, Margaret, Nagel, Katherine I., Ermentrout, G. Bard, Crimaldi, John P., Victor, Jonathan D., 2018. Information-theoretic analysis of realistic odor plumes: What cues are useful for determining location? PLoS Comput. Biol. 14 (7), e1006275.

Bovet, Pierre, Benhamou, Simon, 1988. Spatial analysis of animals' movements using a correlated random walk model. J. Theoret. Biol. 131 (4), 419–433.

Brokaw, Alyson F., Davis, Evynn, Page, Rachel A., Smotherman, Michael, 2021. Flying bats use serial sampling to locate odour sources. Biol. Lett. 17 (10), 20210430.

Cardé, Ring T., 2021. Navigation along windborne plumes of pheromone and resource-linked odors. Annu. Rev. Entomol. 66, 317–336.

Cardé, Ring T., Willis, Mark A., 2008. Navigational strategies used by insects to find distant, wind-borne sources of odor. J. Chem. Ecol. 34, 854–866.

Cassiani, Massimo, Bertagni, Matteo B., Marro, Massimo, Salizzoni, Pietro, 2020. Concentration fluctuations from localized atmospheric releases. Bound.-Layer Meteorol. 177, 461–510.

Catania, Kenneth C., 2013. Stereo and serial sniffing guide navigation to an odour source in a mammal. Nature Commun. 4 (1), 1441.

Celani, Antonio, Villermaux, Emmanuel, Vergassola, Massimo, 2014. Odor landscapes in turbulent environments. Phys. Rev. X 4 (4), 041015.

Connor, Erin G., McHugh, Margaret K., Crimaldi, John P., 2018. Quantification of airborne odor plumes using planar laser-induced fluorescence. Exp. Fluids 59, 1–11.

Crimaldi, J.P., 2008. Planar laser induced fluorescence in aqueous flows. Exp. Fluids 44, 851–863.

Crimaldi, John, Lei, Hong, Schaefer, Andreas, Schmuker, Michael, Smith, Brian H., True, Aaron C., Verhagen, Justus V., Victor, Jonathan D., 2022. Active sensing in a dynamic olfactory world. J. Comput. Neurosci. 50 (1), 1–6.

Crimaldi, John P., Wiley, Megan B., Koseff, Jeffrey R., 2002. The relationship between mean and instantaneousstructure in turbulent passive scalar plumes. J. Turbul. 3 (1), 014.

Demir, Mahmut, Kadakia, Nirag, Anderson, Hope D., Clark, Damon A., Emonet, Thierry, 2020. Walking drosophila navigate complex plumes using stochastic decisions biased by the timing of odor encounters. Elife 9, e57524.

Fackrell, J.E., Robins, A.G., 1982. The effects of source size on concentration fluctuations in plumes. Bound.-Layer Meteorol. 22 (3), 335–350.

Findley, Teresa M., Wyrick, David G., Cramer, Jennifer L., Brown, Morgan A., Holcomb, Blake, Attey, Robin, Yeh, Dorian, Monasevitch, Eric, Nouboussi, Nelly, Cullen, Isabelle, et al., 2021. Sniff-synchronized, gradient-guided olfactory search by freely moving mice. Elife 10, e58523.

Gadenne, Christophe, Barrozo, Romina B., Anton, Sylvia, 2016. Plasticity in insect olfaction: to smell or not to smell? Annu. Rev. Entomol. 61, 317–333.

Gumaste, Ankita, Baker, Keeley L., Izydorczak, Michelle, True, Aaron C., Vasan, Ganesh, Crimaldi, John P., Verhagen, Justus, 2024. Behavioral discrimination and olfactory bulb encoding of odor plume intermittency. Elife 13, e85303.

Gumaste, A., Coronas-Samano, G., Hengenius, J., Axman, R., Connor, E.G., Baker, K.L., Ermentrout, B., Crimaldi, J.P., Verhagen, J.V., 2020. A comparison between mouse, in silico, and robot odor plume navigation reveals advantages of mouse odor tracking. Eneuro 7 (1).

Hengenius, James B., Connor, Erin G., Crimaldi, John P., Urban, Nathaniel N., Ermentrout, G. Bard, 2021. Olfactory navigation in the real world: Simple local search strategies for turbulent environments. J. Theoret. Biol. 516, 110607.

Hunt, G.R., Van den Bremer, T.S., 2011. Classical plume theory: 1937–2010 and beyond. IMA J. Appl. Math. 76 (3), 424–448.

Izquierdo, Eduardo J., Beer, Randall D., 2013. Connecting a connectome to behavior: an ensemble of neuroanatomical models of C. elegans klinotaxis. PLoS Comput. Biol. 9 (2), e1002890.

Jones, Peter W., Urban, Nathan N., 2018. Mice follow odor trails using stereo olfactory cues and rapid sniff to sniff comparisons. BioRxiv 293746.
Kajiura, Stephen M., Forni, Jesica B., Summers, Adam P., 2005. Olfactory morphology of carcharhinid and sphyrnid sharks: does the cephalofoil confer a sensory advantage? J. Morphol. 264 (3), 253–263.
Kikuta, Shu, Sato, Kenichiro, Kashiwadani, Hideki, Tsunoda, Koichi, Yamasoba, Tatsuya, Mori, Kensaku, 2010. Neurons in the anterior olfactory nucleus pars externa detect right or left localization of odor sources. Proc. Natl. Acad. Sci. 107 (27), 12363–12368.
Laska, Matthias, 2017. Human and animal olfactory capabilities compared. In: Springer Handbook of Odor. Springer, pp. 81–82.
Lei, Hong, Riffell, Jeffrey A., Gage, Stephanie L., Hildebrand, John G., 2009. Contrast enhancement of stimulus intermittency in a primary olfactory network and its behavioral significance. J. Biol. 8, 1–15.
Liao, Qian, Cowen, Edwin A., 2002. The information content of a scalar plume–A plume tracing perspective. Environ. Fluid Mech. 2, 9–34.
Liu, Annie, Papale, Andrew E., Hengenius, James, Patel, Khusbu, Ermentrout, Bard, Urban, Nathan N., 2020. Mouse navigation strategies for odor source localization. Front. Neurosci. 14, 218.
Louis, Matthieu, Huber, Thomas, Benton, Richard, Sakmar, Thomas P., Vosshall, Leslie B., 2008. Bilateral olfactory sensory input enhances chemotaxis behavior. Nature Neurosci. 11 (2), 187–199.
Lozano, A., Yip, B., Hanson, R.K., 1992. Acetone: a tracer for concentration measurements in gaseous flows by planar laser-induced fluorescence. Exp. Fluids 13 (6), 369–376.
Machens, Christian K., Romo, Ranulfo, Brody, Carlos D., 2005. Flexible control of mutual inhibition: a neural model of two-interval discrimination. Science 307 (5712), 1121–1124.
Martin, Joshua P., Beyerlein, Aaron, Dacks, Andrew M., Reisenman, Carolina E., Riffell, Jeffrey A., Lei, Hong, Hildebrand, John G., 2011. The neurobiology of insect olfaction: sensory processing in a comparative context. Prog. Neurobiol. 95 (3), 427–447.
Martinez, Dominique, 2014. Klinotaxis as a basic form of navigation. Front. Behav. Neurosci. 8, 275.
Matheson, Andrew M.M., Lanz, Aaron J., Medina, Ashley M., Licata, Al M., Currier, Timothy A., Syed, Mubarak H., Nagel, Katherine I., 2022. A neural circuit for wind-guided olfactory navigation. Nature Commun. 13 (1), 4613.
McKay, Michael D., Beckman, Richard J., Conover, William J., 2000. A comparison of three methods for selecting values of input variables in the analysis of output from a computer code. Technometrics 42 (1), 55–61.
Michaelis, Brenden T., Leathers, Kyle W., Bobkov, Yuriy V., Ache, Barry W., Principe, Jose C., Baharloo, Raheleh, Park, Il Memming, Reidenbach, Matthew A., 2020. Odor tracking in aquatic organisms: the importance of temporal and spatial intermittency of the turbulent plume. Sci. Rep. 10 (1), 7961.
Moore, Paul, Crimaldi, John, 2004. Odor landscapes and animal behavior: tracking odor plumes in different physical worlds. J. Mar. Syst. 49 (1–4), 55–64.
Murlis, John, Elkinton, Joseph S., Carde, Ring T., et al., 1992. Odor plumes and how insects use them. Annu. Rev. Entomol. 37 (1), 505–532.
Murlis, John, Willis, Mark A., Cardé, Ring T., 2000. Spatial and temporal structures of pheromone plumes in fields and forests. Physiol. Entomol. 25 (3), 211–222.
Nironi, Chiara, Salizzoni, Pietro, Marro, Massimo, Mejean, Patrick, Grosjean, Nathalie, Soulhac, Lionel, 2015. Dispersion of a passive scalar fluctuating plume in a turbulent boundary layer. Part I: Velocity and concentration measurements. Bound.-Layer Meteorol. 156, 415–446.
Ottino, Julio M., et al., 1990. Mixing, chaotic advection, and turbulence. Annu. Rev. Fluid Mech. 22 (1), 207–254.
Parabucki, Ana, Bizer, Alexander, Morris, Genela, Munoz, Antonio E., Bala, Avinash D.S., Smear, Matthew, Shusterman, Roman, 2019. Odor concentration change coding in the olfactory bulb. Eneuro 6 (1).
Park, In Jun, Hein, Andrew M., Bobkov, Yuriy V., Reidenbach, Matthew A., Ache, Barry W., Principe, Jose C., 2016. Neurally encoding time for olfactory navigation. PLoS Comput. Biol. 12 (1), e1004682.
Rabell, José Esquivelzeta, Mutlu, Kadir, Noutel, João, Del Olmo, Pamela Martin, Haesler, Sebastian, 2017. Spontaneous rapid odor source localization behavior requires interhemispheric communication. Curr. Biol. 27 (10), 1542–1548.
Rajan, Raghav, Clement, James P., Bhalla, Upinder S., 2006. Rats smell in stereo. Science 311 (5761), 666–670.
Reddy, Gautam, Murthy, Venkatesh N., Vergassola, Massimo, 2022. Olfactory sensing and navigation in turbulent environments. Annu. Rev. Condens. Matter Phys. 13, 191–213.
Richardson, Lewis Fry, 1926. Atmospheric diffusion shown on a distance-neighbour graph. Proc. R. Soc. Lond. Ser. A, Contain. Pap. Math. Phys. Character 110 (756), 709–737.
Riffell, Jeffrey A., Abrell, Leif, Hildebrand, John G., 2008. Physical processes and real-time chemical measurement of the insect olfactory environment. J. Chem. Ecol. 34, 837–853.
Rigolli, Nicola, Magnoli, Nicodemo, Rosasco, Lorenzo, Seminara, Agnese, 2022a. Learning to predict target location with turbulent odor plumes. Elife 11, e72196.
Rigolli, Nicola, Reddy, Gautam, Seminara, Agnese, Vergassola, Massimo, 2022b. Alternation emerges as a multi-modal strategy for turbulent odor navigation. Elife 11.
Ritsch, Colter C., 2019. Experimental Quantification of Spatiotemporal Structure of Scalar Plumes Using Planar Laser-Induced Fluorescence. University of Colorado at Boulder.
Roberts, Philip J.W., Webster, Donald R., 2002. Turbulent diffusion. In: Environmental Fluid Mechanics-Theories and Application. ASCE Press, Reston, Virginia, pp. 7–47.
Shpiro, Asya, Curtu, Rodica, Rinzel, John, Rubin, Nava, 2007. Dynamical characteristics common to neuronal competition models. J. Neurophysiol. 97 (1), 462–473.
Talley, Jennifer L., White, Edward B., Willis, Mark A., 2023. A comparison of odor plume-tracking behavior of walking and flying insects in different turbulent environments. J. Exp. Biol. 226 (2), jeb244254.
Taylor, Geoffrey I., 1922. Diffusion by continuous movements. Proc. Lond. Math. Soc. 2 (1), 196–212.
Verano, Kyrell Vann B., Panizon, Emanuele, Celani, Antonio, 2023. Olfactory search with finite-state controllers. Proc. Natl. Acad. Sci. 120 (34), e2304230120.
Vergassola, Massimo, Villermaux, Emmanuel, Shraiman, Boris I., 2007. 'Infotaxis' as a strategy for searching without gradients. Nature 445 (7126), 406–409.
Vickers, Neil J., 2000. Mechanisms of animal navigation in odor plumes. Biol. Bull. 198 (2), 203–212.
Victor, Jonathan D., Boie, Sebastian D., Connor, Erin G., Crimaldi, John P., Ermentrout, G. Bard, Nagel, Katherine I., 2019. Olfactory navigation and the receptor nonlinearity. J. Neurosci. 39 (19), 3713–3727.
Villermaux, Emmanuel, 2019. Mixing versus stirring. Annu. Rev. Fluid Mech. 51 (1), 245–273.
Wachowiak, Matt, 2011. All in a sniff: olfaction as a model for active sensing. Neuron 71 (6), 962–973.
Webster, D.R., Weissburg, M.J., 2001. Chemosensory guidance cues in a turbulent chemical odor plume. Limnol. Oceanogr. 46 (5), 1034–1047.
Weiss, Shennan A., Preuss, Thomas, Faber, Donald S., 2008. A role of electrical inhibition in sensorimotor integration. Proc. Natl. Acad. Sci. 105 (46), 18047–18052.
Wilson, D.J., Robins, A.G., Fackrell, J.E., 1985. Intermittency and conditionally-averaged concentration fluctuation statistics in plumes. Atmos. Environ. (1967) 19 (7), 1053–1064.
Wu, Yuli, Chen, Kepu, Ye, Yuting, Zhang, Tao, Zhou, Wen, 2020. Humans navigate with stereo olfaction. Proc. Natl. Acad. Sci. 117 (27), 16065–16071.
Yee, Eugene, 1990. The shape of the probability density function of short-term concentration fluctuations of plumes in the atmospheric boundary layer. Bound.-Layer Meteorol. 51, 269–298.